Mass models and the spiral arms of the Milky Way

Edvin Zigmanovic

Lund Observatory
Lund University

2016-EXA103

Degree project of 60 higher education credits (for a degree of Master)
May 2016

Supervisor: Paul McMillan

Lund Observatory
Box 43
SE-221 00 Lund
Sweden

Abstract

I investigate to what extent spiral arms might affect axisymmetric Galactic models. As we need fully dynamical and high resolution Galactic evolutionary models to probe the structure of the dark matter halo, it is important that we use accurate mass models describing the MW structure. Before reaching to that level of effort, a great deal can be learned from fitting mass and kinematic models to data. Because many researchers still use models which do not include any spiral structure, they might have systematic errors from their models. I therefore compare an axisymmetric model of the Galaxy to a model with added spiral perturbations. The latter was found by adding radial and azimuthal velocity perturbations from an analytic model of spiral structure to a model of the circular velocity of the MW derived from assuming a gravitational potential with an axisymmetric bulge and disk and a logarithmic halo.

Recently and accurately measured distances, proper motions and radial velocities of ~ 100 Galactic maser sources and radial velocity data from the ISM were used to constrain the models. Using the cold gas as tracer objects in the Galaxy allows me to approximate their motions as near-circular and within the plane ($z = 0$).

I use a Bayesian statistical analysis (with a set of priors from a variety of sources) and a Markov Chain Monte Carlo approach to investigate the parameter space of the models to arrive at a set of best fitting parameters for the two models. The resulting probability distributions for all the model parameters and the best-fitting models can then be compared and the question of spiral influence can be answered.

The simple models employed in this thesis work show that including spiral perturbations does modestly change some resulting probability distributions of the model parameters and the best-fitting models. For example, I find a local DM density $\rho_{\mathrm{DM}} = 0.0096 \pm 0.001 \, M_\odot \, \mathrm{pc}^{-3}$ for all models except for the four armed model with spiral perturbations for which $\rho_{\mathrm{DM}} = 0.00917 \pm 0.001 \, M_\odot \, \mathrm{pc}^{-3}$. However, these systematic differences are smaller than their corresponding statistical difference given my amount of data ($\sim$100 masers). As the amount of data increases, the statistical uncertainty will shrink (while there is no reason to expect that the systematic one will). Therefore studies of this kind will be increasingly important as the amount of data improves. I also show that choosing between a two and four armed spiral arm model gives different radial and azimuthal perturbations. For the two armed model, the radial velocity perturbation is vanishing whilst the azimuthal velocity perturbation is significant and the opposite is true for the four armed model. The point is not to derive any accurate numbers but to highlight that there is a difference for even the simplest models and simplest assumptions.

Acknowledgments

I would deeply like to thank my supervisor Dr. Paul McMillan for the great support and guidance throughout this thesis work. I have gotten tremendous insights into using observations to constrain models of the Galaxy and learning about how that ties in to answering big questions about our Universe. I will remember the wonderfully inspiring times and and meetings we shared. It was truly a pleasure and delight working with you.

I would also like to thank all the people at the department, you are lovely people and it was a pleasure to share and discuss ideas with you. I would especially like to thank the people who put together the amazing masters program at Lund Observatory and keep it running. This is not a place where one comes only to sit and do coursework but a place where one gets to partake in weekly seminars, journal clubs, group meetings and much more. It really tickles the brain and keeps the motivation high. I am looking forward to go out in the world with this great experience under my belt.

Populärvetenskaplig beskrivning

Människan har sedan urminnes tider tittat upp mot himlen och försökt lista ut vår plats i Universum. Vi har kommit långt fram sedan tiderna man kartlade stjärnors positioner för hand, till att använda superdatorer till att simulera kosmisk historia.

Just nu befinner vi oss i en era där stora resurser läggs ner på att studera vårt hem, vår galax, Vintergatan, i mycket större detalj än förr. En av dessa projekt är Gaia satelliten, vars mål är att mäta positioner, hastigheter och ljusstyrkor av en miljard stjärnor i Vintergatan med högre precision än någonsin. Gaia kommer säkerligen att revolutionera vår förståelse av galaxers uppbyggnad, struktur och formationshistorik. Det är i frammarchen av precision som mitt arbete kommer in. Med allt mer inkommande detaljerad data kommer behovet av allt mer detaljerade matematiska modeller av Vintergatan fram.

Alla miljarder stjärnor och all gas i Vintergatan kretsar i stort sätt kring dess mitt punkt som råkar vara ett gigantiskt svart hål. Det tar c.a. tjugo miljarder år för en typisk stjärna i solens område att ta sig ett varv kring galaxcentrum. Detta system är dessutom insvept i ett så kallat halo av mörk materia, något som man inte direkt kan detektera men något som astronomer tros finnas då det skulle förklara en hel del annars oförklarliga observationer. Astronomer har observerat många delar av Vintergatan och bevisen pekar på att det finns så kallade spiral armar. Dessa är regioner där gas och stjärnor är mer ihoptryckta än de annars skulle vara utanför en arm. Det är många som försöker finna ut varför dessa spiralarmar existerar och varför andra galaxer har olika många. Det råder fortfarande ingen konsensus i dessa frågor.

Det är inte bara ur empirisk data man kan dra slutsatser om hur världen runt om kring oss fungerar utan även ur de matemetiska modellerna som beskriver fenomenen. Genom att anta en modell för ett system kan man beräkna olika kvantiteter från den och sedan jämföra resultaten med det man kan observera i verkligheten. Man kan på så sätt validera teorier beroende på hur bra modellen förutsäger mätvärden i verkligheten.

Jag har försökt besvara frågan: Påverkar modeller av spiralarmar gamla modeller utan dem? För att besvara denna fråga har jag använt en typisk modell för Vintergatans struktur och jämfört den med samma modell där jag lägger till spiral armar. Jag har använt observationell data från högenergiska gasområden i Vintergatan för att urskilja de matematiska modellerna. Jag har implementerat en statistisk metod som möjliggör användningen av tidigare beräknade kvantiteter som beskriver Vintergatan och en algoritm som letar bland alla modellparametrar för att hitta de som passar bäst. Genom att titta på vilka olika parametrar de olika modellerna föredrar kan jag dra slutsatser om hurvida skildrade de är.

Mina resultat visar på att man borde utveckla mina modeler eftersom det finns underlag som tyder på att spiralarmar kan förändra egenskaper i Vintergatan. Genom att inkludera spiralarmar förutsäger man till exempel en lägre koncentration av mörk materia nära vår sol. Detta resultat är viktigt då många vetenskapliga studier och experiment i världen hänger på att veta detta värde i så noga utsträckning som möjligt. Det är mycket som kommer att förändras när man börjar ta hänsyn till spiralarmar i detaljerade modeller och jag hoppas att fler börjar att inkludera dessa i deras modeller.

Contents

List of Figures

List of Tables

Chapter 1

Introduction

Even though a wealth of knowledge about the properties of galaxies has accumulated over the last 100 years, a great deal is still unknown. Many have taken on the endeavor, and rightly so, to continue in the quest of bettering the understanding of our own Galaxy. Simple questions, such as: how many spiral arms are there, how is the dark matter distributed, how do the spiral arms affect Galactic objects, are still up for debate. These are key features which, when understood, may tell us about how the Universe works in a very fundamental way. We aim to make use of the great advantage of residing in a galaxy, our home, the Milky Way (MW). From within, we can probe, in detail, the properties of Galactic objects and therefore test our models, to a great accuracy. Once refined, we hope that the locally developed models will teach about the rest of the Universe.

In this thesis, I aim to show to what extent spiral arms affect models of the MW's gravitational potential. This should encourage the community to be more careful when choosing models of the Galaxy as it will become apparent that spiral arms could alter results. Of course, a more accurate model will allow for a better determination of the dark matter content and predictions of the future motions of stars and gas within the Galaxy than previous models. With Gaia, the European astrometric satellite (Lindegren et al. 2012) due to provide a map of the positions and velocities of a billion stars in the MW, it is vital to ensure that our modeling techniques are able to cope with the effects of perturbations like spiral arms.

The main concept used in this work is to, from an underlying model of the MW gravitational potential, calculate the expected velocity of Galactic objects and compare them to observational data. These were proper motions and radial velocities of Galactic maser sources (Reid et al. 2014) and terminal velocities from the interstellar medium (ISM), as traced by HI emission lines (Malhotra 1995). Combining the constraints from the data with a handful of parameters from previous studies, a set of best fitting parameters were determined. This is called forward modeling. In this regime, I have compared the resulting best fitting parameters with different models of the MW's gravitational potential. Most importantly, models with and without spiral arms.

Chapter 2

Background

When Paczynski (1990) set out to determine the distribution of gamma-ray burst progenitors, he set up a model for the gravitational potential of the MW in order to numerically integrate the progenitor's orbit. Efforts like his are common. When one wishes to determine distributions, future motions or birth locations of stars and gas, it is necessary to assume a model for the gravitational potential. From here, one is able to calculate the mutual accelerations of each object from which one is further able to convert into velocity components. Once the expected velocity components of an object, given its position on the sky, are calculated with a given model for the gravitational potential, it can be compared to its corresponding observational velocity components. The validity of a model can as such be tested.

Models of galactic gravitational potentials are as such used for many purposes e.g. associating Galactic objects with velocity components, tracing stars back to their birth location, calculating the local dark matter density etc. It is therefore of great interest to develop a well fitting model such to describe nature as well as possible. A part of this work is therefore to study the importance of spiral structure.

Any model of the MW's gravitational potential greatly depends on the structure of the system. As more and more data is being gathered with time, more and more details about its structure are revealed. It is with the detailed knowledge of the structure of the MW one can aim to best represent it in a model for its corresponding gravitational potential. A brief overview of Galactic structure is therefore given as a prequel to the model presented in this thesis work.

2.1   The Galactic structure

The billions of stars residing in the MW tend not to arrange themselves as homogeneously as gas particles in a beach ball would, but rather exist in somewhat loosely defined groups. Crudely, but to a relatively good approximation, the stellar contents of our Galaxy can be thought of as comprising two main parts, a central bulge and a disk as sketched in Figure 2.1. It is perfectly reasonable to model their structure individually and then combine them.
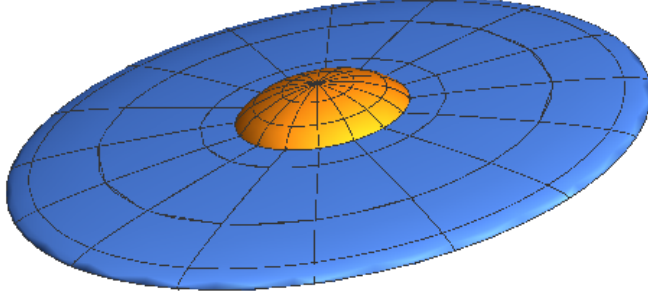
Figure 2.1: A representation of the Milky Way where the disk is shown in blue and bulge in orange.

2.1.1 The Galactic bulge

In a cosmology where galaxies are formed by hierarchical growth, the bulge is a region where an older stellar population resides. This view is supported by the observationally determined age of the bulge population. The main tracer population for the age determination are the red clump giant stars (RCG). These stars have evolved off of their main sequence and their stellar evolution are best fitted to isochrones of order ~ 10 Gyr old (Clarkson et al. 2008).

Based on ~ 8 million bulge RCGs from the VVV survey (Minniti et al. 2010), Wegg & Gerhard (2013) found a fitting density map that has peanut-like structure. Basically, the bulge is bar-shaped where the longest axis lies in the midplane but above ~ 400 pc off of the midplane, the bulge takes on the shape of an X. Furthermore, they found an angle between the tip of the bar and the line of sight to the Galactic Center (GC) of $(27 \pm 2)°$.

For the purpose of this thesis, such details are neglected as they are complicated to solve analytically. Instead, I assume a simple oblate spheroidal shape where the longer axes are parallel with the Galactic plane as seen in 2.1. Approximating the bulge to a spheroid should not affect the goal of this thesis, which is to use objects far away from the bulge region to investigate the perturbations induced by spiral arms.

Using photometric data of bulge RCGs, Bissantz & Gerhard (2002) found a best-fitting stellar density model of the bulge that follows a mix between an exponential and a power-law distribution. For a spheroidal model, McMillan (2011) reduces the model to the following bulge density profile

$$\rho_{\rm b} = \frac{\rho_{\rm b,0}}{(1 + r'/r_0)^\alpha} \exp\left[-(r'/r_{\rm cut})\right]^2 \tag{2.1}$$

where $\rho_{b,0}$ is the scale density, $r' = \sqrt{R^2 + (z/q)^2}$ is in cylindrical coordinates where $q = 0.5$ is the axis ratio of the spheroid, $r_{\rm cut} = 2.1$ kpc, $r_0 = 0.075$ kpc and $\alpha = 1.8$. The best fitting bulge mass for their model was $M_b = (8.9 \pm 2) \times 10^9 \, M_\odot$.

2.1.2 The Galactic disk

From studying the chemistry and distribution of stars in the Galactic disk, one is able to argue that the disk ought to be subdivided into a thin and a thick disk component (Bensby et al. 2003; Jurić et al. 2008).

The thin (t) disk hosts the younger (on average) stars, which are concentrated to the Galactic midplane. Conversely, the thick (T) disk is inhabited by an older stellar population, for which the stars are more extended in z direction.

A commonly accepted disk density profile is described by a double exponential model

$$\rho_{\mathrm{d}}(R, z) = \frac{\Sigma_{\mathrm{d},0}}{2z_{\mathrm{d}}} \exp\left[-\frac{|z|}{z_{\mathrm{d}}} - \frac{R}{R_{\mathrm{d}}}\right] \tag{2.2}$$

where z_{d} is the scale height, R_{d} is the scale length and $\Sigma_{\mathrm{d},0}$ is the surface scale density. The total mass for such a disk becomes $M_{\mathrm{d}} = 2\pi\Sigma_{\mathrm{d},0}R_{\mathrm{d}}^2$.

By mapping the number density distribution of $\sim$28 million stars in the MW from the Sloan Digital Sky Survey, Jurić et al. (2008) found best fitting scale heights and lengths for the double exponential model with a quoted 20% accuracy. The resulting scale heights were $z_{\mathrm{d}}^t = 300$ pc and $z_{\mathrm{d}}^T = 900$ pc and the scale lengths $R_{\mathrm{d}}^t = 2.6$ kpc and $R_{\mathrm{d}}^T = 3.6$ kpc. The stellar mass for the thin disk $M^t = 4 \pm 1 \times 10^{10}\ M_{\odot}$ and for the thick disk $M^T \approx 0.2M^t$.

2.1.3 The Halo

Hosting all of the aforementioned components is a dark matter (DM) halo. In the standard cosmological picture, galaxies and galaxy clusters are baryonic[1] blips embedded in DM halos. The existence of these halos are motivated from observing the motions of stellar populations away from the disk region, gaseous rotation curves, gravitational lensing effects and simulations, all of which require stronger gravitational fields which the baryons alone cannot induce (Zwicky 1937; van der Kruit & Freeman 1984; Kleyna et al. 2001; Adams et al. 2012; Freeman 1970; Bosma et al. 1977; Rubin et al. 1980; van Albada et al. 1985; Walsh et al. 1979; Clowe et al. 2006; Dubinski & Carlberg 1991; Navarro et al. 1996; Stadel et al. 2009; Springel et al. 2008; Dehnen & Read 2011).

Dark Matter

The simple and classical way to infer the existence of DM is by looking at the velocity distribution of gas far from the galactic center as a function of its galactocentric radius R. One would expect the circular velocity (far from the disk) to decay as $V \sim \sqrt{M/R}$ from Newtonian dynamics. However, observations points to the contrary (Begeman et al. 1991).

Figure 2.2 shows the velocity distribution of neutral hydrogen gas in NGC6503, which clearly shows that the circular velocity of the gas at large radii is constant. By looking at the aforementioned Newtonian formula, to compensate the increasing R, an increasing mass M is required in order to keep the velocity distribution constant, which is not luminous. It is therefore permissible to assume the existence of another kind of matter that is beyond current direct observational techniques. This currently undetected material is named dark matter (DM).

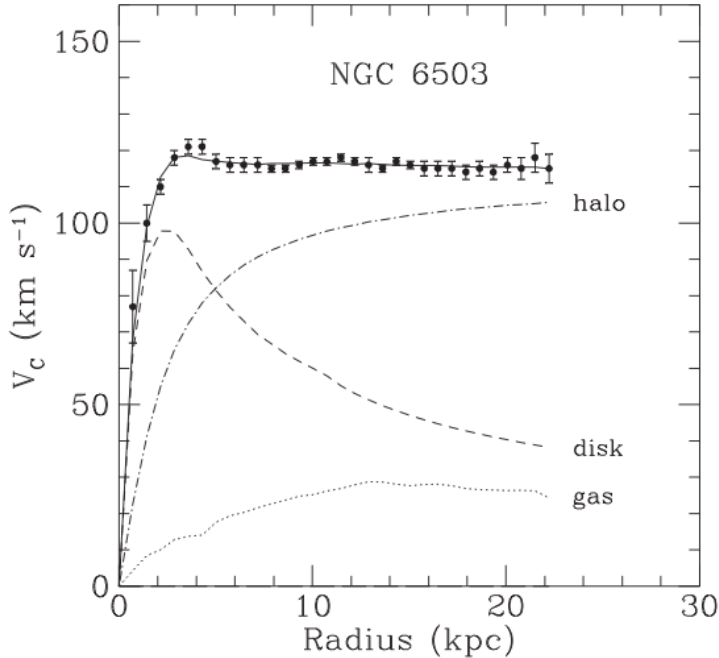[1]Baryons: Particles from the standard model (SM) of particle physics.

Figure 2.2: The circular velocity of 21-cm neutral hydrogen lines of NGC6503 as a function of Galactocentric radius (Begeman et al. 1991). The data points (solid dots) fit with a model of the circular velocity once all the dashed components are added together.

Large scale stellar surveys reveal the structural complexity of the halo. It has multiple components and substructures, all of which engulf smaller galaxies and tidally disrupt them (Ibata et al. 1997; Belokurov et al. 2006; Schlaufman et al. 2009).

As the window of theoretical speculation was opened in the search for a DM model, there have been many suggestions. One of them, has been rather successful in reproducing today's Universe in cosmological simulations (Springel et al. 2006; Guo et al. 2011). The successful model requires the DM to be dynamically cold (CDM) and its individual particle constituents to be weakly interacting and massive (WIMP). DM particles with such properties should therefore able to interact via gravity and the weak nuclear force.

As the solar system is moving through the Galaxy, we expect some flux of DM particles. The Large Underground Xenon experiment (LUX) is one of several experiments that aims to directly detect the flux of DM particles on Earth by relying on their assumed weak nuclear interaction with standard model (SM) particles. LUX has deployed a large chamber of 370 kg of liquid Xenon ~ 1.6 km below Earth's surface. The team hopes that the achieved sensitivity of the experimental set up might realize a signal coming from a DM/SM interaction. However, no such signal has yet been detected but constraints have been found, ruling some DM particle candidates out. This endeavor remains alive as significant upgrades to the detector awaits, continuing the search.

In cosmological simulations, the most widely used DM mass density profile, enabling the successful reproductions of observational data as it approximates the density profiles of galaxy

and cluster halos very well, is the Navarro-Frenk-White (NFW) profile (Navarro et al. 1996)

$$\rho_{\mathrm{h}} = \rho_{\mathrm{h},0}(r/r_s)^{-1}(1 + r/r_s)^{-2}$$

where $\rho_{\mathrm{h},0}$ is a scale density and r_{s} is a scale radius. The density behaves as $\rho \propto r^{-1}$ in the core and as $\rho \propto r^{-3}$ on the outskirts. However, despite the accuracy of the NFW density profile, a different expression for the halo profile will be used in this thesis work due to its simplicity and speed of use (section 3.1, Eq. (3.3)).

One of the ways to test our understanding of DM is to calculate the DM mass density in a local volume (few 100 pc). Within such a volume, we are able to relatively accurately measure the kinematics of stars. From these kinematic data sets and density profiles, a local mass density can be estimated. By disentangling the baryonic mass contribution from that of the DM, we can estimate a local DM density $\rho_{\mathrm{DM},0}$. The numerical value of this parameter plays an important role to the particle physics community. As mentioned, there are great efforts to measure the flux of DM on Earth and formulas used to calculate the rate of interaction require the local DM density as input. Currently, estimates for $\rho_{\mathrm{DM},0}$ range from ≈ 0.006 to ≈ 0.02 $M_{\odot}\,\mathrm{pc}^{-3}$ (McMillan 2011; Bovy & Tremaine 2012; Garbari et al. 2012; Zhang et al. 2013; Bovy & Rix 2013; Salucci et al. 2010).

A standardized way of characterizing the extent of the halo is to restrict the radius to where the density is 200 times the critical density, $\rho_{200} = 200\rho_{\mathrm{crit}} \Rightarrow r_{200}$. The critical density is the density of the Universe if its geometry was flat, i.e. no space-time curvature. Locally, $\rho_{\mathrm{crit}} = 3H_0^2/8\pi G$ where H_0 is the Hubble constant ($H_0 \approx 73\,\mathrm{kms}^{-1}\mathrm{Mpc}^{-1}$). The mass M_{200} can be defined within this region. Based on the kinematics of halo stars, the mass is estimated $M_{200} = 1 - 2 \times 10^{12}\,M_{\odot}$ (Kafle et al. 2012; Deason et al. 2012) and by modeling local observables (McMillan 2011).

Another property of the halo is its shape. In simulations, where baryons are included, the halo takes on a triaxial-oblate shape (Kazantzidis et al. 2004; Bailin et al. 2005; Abadi et al. 2010). The same conclusion can be drawn when fitting models of halo shapes to observational data of streams from tidally disrupted dwarf galaxies. Such observations have yielded $q = 0.95 \pm 0.15$ (essentially spherical) where q defines the axis ratio between the z axis and the plane (Koposov et al. 2010; Küpper et al. 2015).

2.2 Spiral arms

Galactic spirals arms can be regarded as regions where matter is temporarily compressed due to passing density waves. As it turns out, such density waves and material in the disk do not generally rotate at the same rate. Therefore, gas that pass the waves (or gets passed by a wave) is compressed, allowing gravitational collapse of the gas to ensue at a faster rate, triggering star formation (SF).

A simple model of the spiral structure is to assume them to be long-living and static. In other words, the wave pattern rotates with a fixed pattern speed over orbital periods. This concept was made popular by Lin & Shu (1964) where the surface density of the disk took on the form of a wave equation. Such a model is usually referred to as the stationary spiral structure and it clearly departs from a picture of a smooth triaxial shape of the disk.

Other authors have argued that spiral arms are a transient phenomenon (Grand et al. 2012; Grand & Kawata 2015; Pérez-Villegas et al. 2015). In this picture, as a galaxy evolves

in time, arms can get 'destroyed' and 'recreated', giving them a transient nature.

The interplay of stars and density waves can be rather complex due to a star's susceptibility of being dynamically heated by such a wave. As an arm is a region of of temporarily compressed matter, any star trailing the arm will experience a greater gravitational attraction towards it. Therefore, as angular momentum is changed, they radially migrate outwards in the disk. On the contrary, if the arm is trailing a star, the star experiences deceleration and radially migrates inward. For these reasons, and the fact that stars have vertical motion, modeling the orbits of stars can become very complex. More importantly, radially migrating stars strongly depart from a simple near-circular orbit.

Gas, on the other hand, is much more efficient at dissipating energy in all directions and can thus reconfiguring its energetic state such to remain on a near-circular orbit (Baba et al. 2016) and moreover, stay in the mid-plane of the disc. Therefore, if one is to make a model relying on objects following a near-circular orbit and residing at $z \approx 0$, gas is a more favorable tracer than stars.

2.2.1 Masers

A maser is the microwave analogy of a laser. It is a coherent light source emitted by molecules commonly found in molecular clouds or High Mass Star Forming Regions (HMSFRs). It is the abundance of energetic radiation in HMSFRs that power the masers. By definition, the narrow frequency range radiated by a maser makes for an excellent tracer target. The typical wavelength of a maser if of order GHz and typical sources are OH, H_2O and NH_3.

With spirals arms as the main birth location for stars, the measured parallax, proper motion and radial velocity of masers can thus be mapped and serve as proxies for identifying the location and kinematics of spiral arms. This has in fact been done. Figure 2.3 shows a face on view of the MW where the points indicate the location of ~ 100 maser sources (Reid et al. 2014).
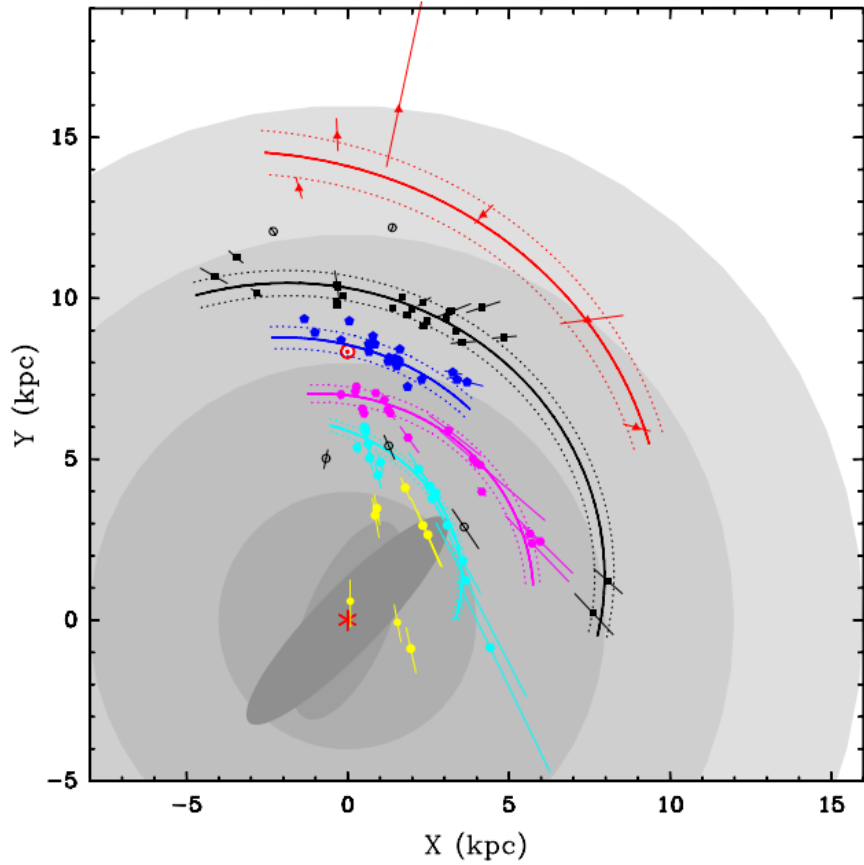
Figure 2.3: Plan view of the MW where the points represent maser sources (Reid et al. 2014).

As such, this group find strong evidence for the existence of spiral arms in the MW based on the parallaxes and proper motions from masers as observed by The Bar and Spiral Structure Legacy Survey[2](BeSSeL) and the Japanese VLBI Exploration of Radio Astronomy [3] (VERA). The accuracies of the measurements are typically $\pm 20\,\mu$as with some as accurate as $\pm 5\,\mu$as.

2.3 The value of having a model and studying the MW

A good theory that describes parts of our natural world is one which can be written down in mathematical form. The answers of nature then lie in the forms of the equations and importantly, the values of its constants. By extracting observables from a mathematical model, such as forces, velocities, energies, etc, we are able to test them by comparing them to values that have been retrieved from observations. Creating a model is therefore a powerful tool as it gives insights into the nature of nature.

When it comes to large systems, such as galaxies, it can be useful to assume simple models in order to catch general trends. Analytic models are in a computational sense 'cheap' and large sets of data from surveys can therefore be correlated quickly. We are in this sense able

---

[2]http://bessel.vlbi-astrometry.org
[3]http://veraserver.mtk.nao.ac.jp

to discriminate between models at an early stage before committing to large simulations and dynamical modeling which is an important final step.

It it therefore perfectly reasonable to compare some simple models of the MW (i.e. spiral arms vs no spiral arms) against recent data to get hints into its structure. It is with great pleasure we take advantage of our unique position in the Universe. Here, we can get detailed observations and test models that could otherwise not be testable by extragalactic galaxies.

As mentioned, moving to fully dynamical models and testing their validity is an essential step as most of the mass in galaxies is expected to reside in the DM halo, which fundamentally cannot be probed directly (as of yet). Before a dynamical model can be constructed and tested in simulations, a model describing the distribution of mass is essential to get right because it directly couples to the shape of the gravitational field, which fundamentally governs the motion of the objects residing within it. It is therefore important to show to what extent the inclusion of spiral perturbations in the Galaxy changes important characteristics, such as the mass of the various components.

Chapter 3

Theory

The key concepts that are used to construct the models in this thesis are presented in this section. In section 3.1 I explain how the gravitational potential is set up and crucially, how expressions for the various velocity components are gained from it. In section 3.2 I introduce what could in some respects be regarded as a philosophy that enables one to constrain models by making use of prior studies. Lastly, in section 3.3, I present an algorithm that finds best-fitting parameters to models based on observational data.

3.1 The gravitational potential and the circular velocity

In order to achieve the goal of calculating parameters with which we can later compare to observational data, we must start with some basis of predicting future motion of objects residing in the Galaxy. The basis, in this thesis work, will come from turning the constructed model for the gravitational potential into a model for the gas' circular velocity.

The first step is to realize that the gradient of the gravitational potential Φ is an object's acceleration,

$$\mathbf{a} = -\boldsymbol{\nabla}\Phi.$$

The second, to add the separately modeled components of the Galaxy that are deemed to dominate the gravitational field together. An expression for the total acceleration of a test particle within such a field is then given by

$$\mathbf{a}_{\text{tot}} = -\boldsymbol{\nabla}\sum_{i=1}^{3}\Phi_i, \tag{3.1}$$

where $i = 1, 2, 3$ represent the bulge, disk and halo respectively and the gradient can be expressed in cylindrical coordinates $\boldsymbol{\nabla} = \partial/\partial R\,\hat{\boldsymbol{R}} + 1/R\,\partial/\partial\phi\,\hat{\boldsymbol{\phi}} + \partial/\partial z\,\hat{\boldsymbol{z}}$.

The bulge and the disk are modeled as Miyamoto-Nagai potentials (Miyamoto & Nagai 1975) which has the expression

$$\Phi(R, z) = -\frac{GM}{\sqrt{R^2 + \left(a + \sqrt{z^2 + b^2}\right)^2}}, \tag{3.2}$$

where G is the Newtonian gravitational constant, M represents the total mass contained within a system, R is the radial distance from the Galactic center, z the height above the

plane, a is the scale length and b is the scale height. In short, the parameters a and b determine the shape of a spheroid. The ratio $a/b > 1$ makes an oblate object and $a/b < 1$ makes a prolate object.

The halo component is modeled as a logarithmic potential (Binney & Tremaine 2011)

$$\Phi_3(R, z) = \frac{1}{2} v_0^2 \ln \left(R_c^2 + R^2 + \frac{z^2}{q^2} \right),$$

(3.3)

where q is the axis-ratio, R_c the core radius and v_0 the maximum obtainable velocity in this potential.

By construction, the bulge, described by Φ_1 will contain the mass M_1, the scale length a_1 and the scale height b_1. Similarly, the disk, described by Φ_2, will have a mass M_2, a scale length a_2 and a scale height b_2. The superposition of these components, including the halo will result in the total MW potential

$$\Phi_{\mathrm{MW}} = \Phi_1 + \Phi_2 + \Phi_3.$$

Of course, as discussed in sections 2.1.1 and 2.1.2, the density profile of the disk and bulge have exponential components which departs from the MN model. However, it is stressed that the analytical MN model is applied to data quicker and is therefore more convenient to use as opposed to integrating relatively complicated exponentials when solving Poisson equation $\nabla^2 \Phi = 4\pi G \rho_{\mathrm{exp}}$.

3.2 Bayesian inference

For a set of parameters $\boldsymbol{\theta}$ and a set of data d, one can aim to maximize the likelihood $\mathcal{L}(d|\boldsymbol{\theta})$, by running through the parameter space $\boldsymbol{\theta}$ in order to find a best-fitting model. The Bayesian approach allows one to go beyond that, by making use of prior knowledge of the set of parameters. The new probability distribution, the posterior, is given by:

$$posterior = \frac{likelihood \times prior}{evidence} \iff p(\boldsymbol{\theta}|d) = \frac{\mathcal{L}(d|\boldsymbol{\theta}) \, p(\boldsymbol{\theta})}{p(d)},$$

(3.4)

where $p(\boldsymbol{\theta})$ is the essential new addition which holds the probability of a parameter as determined by previous studies. The probability of the data $p(d)$ is assumed to be a normalization constant here. This is fine because it is the same of all the models.

The probability distributions $\mathcal{L}(d|\boldsymbol{\theta})$ & $p(\boldsymbol{\theta})$ in Eq.(3.4) will take the form of a Gaussian probability distribution function (pdf)

$$f_G(x|\mu, \sigma) = \frac{1}{\sigma\sqrt{2\pi}} \exp\left[-\frac{(x-\mu)^2}{2\sigma^2} \right]$$

(3.5)

where μ represents a mean value or in this case observational data, σ its uncertainty and x a test value obtained from models.

3.2.1 Priors

Below are all of the priors used in order to calculate the Bayesian posterior. The full list of priors used can be seen in Table 4.1.

Bulge mass, M_1

The mass used to represent the bulge, $M_b = (8.9 \pm 2) \times 10^9 \, M_\odot \, (= M_1)$, is taken from McMillan (2011), which, in turn, was obtained from Bissantz & Gerhard (2002). The quoted mass was determined by turning a luminosity density into a mass density, i.e. a mass-to-light ratio (M/L). A best-fitting model for the luminosity density was determined by maximizing the likelihood of a parametric model to two sets of data. The first, near-infrared (NIR) L-band ($\lambda_L = 3 - 4 \, \mu$m) data from the Diffuse Infrared Background Experiment on board the Cosmic Background Explorer satellite (COBE/DIRBE). The second, the line-of-sight distribution of clump giant stars. It is worth noting that the authors assumed a spatially constant M/L-ratio throughout the bulge.

Disk scale length, a_2

As explained in section 2.1.2, galactic disks tend to follow an exponential density profile. Bland-Hawthorn & Gerhard (2016) averaged multiple studies and retrieved a value for the MW disk scale length $R_d = 2.5 \pm 0.4$ kpc. They way the exponential disk parameter R_d is implemented as a prior to constrain the Miyamoto-Nagai scale length a_2 is shown in Appendix C.1. Basically, a ratio between a mass inside and outside R_0 is calculated from both the MN density profile and an exponential disk profile, which are then set to equal. a_2 is then found as a function of R_d.

For b_2, Binney & Tremaine (2011) concluded that the relation $b_2 = 0.2 \, a_2$ fits the light distributions of disk galaxies.

Bulge scale length and height, $a_1 \, \& \, b_1$

The same mass ratio relation as explained above is found for the bulge, this time with the bulge density profile from section 2.1.1. This time, the masses are divided by a bulge cut off radius R_{bc} which indicates the extent of the bulge region. Bissantz & Gerhard (2002) finds the length of the bar to be 3.5 kpc. In this effort, we end up with an expression for the Miyamoto-Nagai scale length a_1 as a function of R_{bc}. The full derivation that can be seen in Appendix C.2. Lastly, $b_1 = 0.5 \, a_1$ (Bissantz & Gerhard 2002).

Vertical force, $F_{z,1.1}$

Kuijken & Gilmore (1991) determined the gravitational force towards the galactic plane at $z = \pm 1.1$ kpc in the Solar neighborhood to $F_{z,1.1} = 2\pi G \times (71 \pm 6) \, M_\odot \, \text{pc}^{-2}$. The authors maximized the likelihood of a kinematic model using 512 K dwarf stars as tracers. As the force in z-direction can be calculated by differentiating my model for the gravitational potential w.r.t. z, these authors' findings are used as a constraint.

Radial force, $F_{R,50}$

Wilkinson & Evans (1999) used the motions of globular clusters and satellite galaxies at Galactocentric radii, R, greater than 20 kpc to determine the mass within 50 kpc of the Galaxy, $M_{R<50 \, \text{kpc}} = (5.4 \pm 1) \times 10^{11} \, M_\odot$. Approximating the Galaxy to be spherically within $R = 50$ kpc, the gravitational force per unit mass can be calculated and used as a constraint in my model; $F_{R,50} = G \times M_{R<50 \, \text{kpc}}/(50 \, \text{kpc})^2 = G \times (2.16 \pm 0.4) \times 10^2 \, M_\odot \, \text{pc}^{-2}$.

Proper motion of the Sun, $\mu_{\mathbf{Sgr\,A^*}}$

Reid & Brunthaler (2004) measured the position of the supermassive black hole Sgr A* with respect to two extragalactic radio sources over an 8 year period, allowing them to infer its proper motion $\mu_{\mathrm{SgrA^*}} = 6.379 \pm 0.024\,\mathrm{mas\,yr^{-1}}$. The apparent proper motion of Sgr A* is assumed to be entirely due to the motion of the Sun and therefore allows one to convert the observed proper motion into a circular velocity for the Sun about the Galactic Center, namely $V_{c,\odot} = \mu_{\mathrm{SgrA^*}}/R_0 = (239 \pm 9)\,\mathrm{km\,s^{-1}}$ where R_0 is assumed to be 8.3 kpc.

3.3 Markov Chain Monte Carlo (MCMC)

Conceptually, the MCMC algorithm is a way of probing a parameter space such that the sets of points produced by the algorithm fairly samples the pdf. This method is invoked as a direct consequence of the lack of computational power to go through a large parameter space in a traditional way.

Computationally, the Markov Chain boils down to the following steps:

1. Let $\boldsymbol{\theta}_n$ represent a point in the parameter space and calculate $p(\boldsymbol{\theta}_n|d)$

2. Choose a trial parameter set $\boldsymbol{\theta}'$ by moving the point $\boldsymbol{\theta}_n$ in all directions in parameter space and calculate $p(\boldsymbol{\theta}'|d)$.

3. Find a random variable r from a uniform distribution in the range [0,1].

4. Check if $p(\boldsymbol{\theta}'|d)/p(\boldsymbol{\theta}_n|d) > r$

   - If true, accept trial parameter set and set a new $\boldsymbol{\theta}_{n+1} = \boldsymbol{\theta}'$.
   - If not, set $\boldsymbol{\theta}_{n+1} = \boldsymbol{\theta}_n$.

5. Go back to step 1 and replace $\boldsymbol{\theta}_n$ with $\boldsymbol{\theta}_{n+1}$

where $p(\boldsymbol{\theta}|d)$ is the posterior from Eq. (3.4).

This algorithm is continually searching for the largest probability. However, critically, the fourth statement allows, sometimes, for a slightly lower probability to be accepted. This ensures that one does not get stuck at a local maximum and that the entire probability space is being probed. In this way, one should find a global maximum along with its deviations from the mean. The first 20 per cent of the number of iterations of this algorithm is discarded and is called 'the burn in phase'. This is common practice because the initially chosen parameters are of course not expected to be correct as stronger deviations from the mean are expected at the start.

This algorithm runs in a loop where each step is given by a new set of test parameters. As such, instead of adding code to the algorithm that would ensure some level of convergence of the parameters which would halt the run, I choose to set at fixed number of iterations at start. In my case, I found that 10^6 iterations gives smooth enough shapes to the resulting Gaussian looking pdfs.

Additionally, to check the robustness of the method, I initialized the algorithm with slightly different values and the results remained unchanged.

Chapter 4

Method

In this section, I show how predicted values of observables, such as radial velocity and proper motion of Galactic objects, can be calculated from models. Furthermore, I show how the observational data is used in order to constrain those models. Given positional data for a Galactic object, the end objective is to calculate its predicted velocity components, which will be obtained from the model of the circular velocity.

From section 3.1 we saw how the total acceleration was calculated from assuming a model for the gravitational potential of the MW. Further assuming that certain Galactic objects (such as gas) have no vertical motion and that they follow a circular orbit lead to the following set of equations,

$$z = 0, \qquad \boldsymbol{\nabla} = \frac{\partial}{\partial R}\, \hat{\boldsymbol{R}}, \qquad \mathrm{a_{tot}} = \sqrt{\mathbf{a_{tot}} \cdot \mathbf{a_{tot}}} = \frac{V_{c,\mathrm{tot}}^2}{R}. \qquad (4.1)$$

Combining Equations (3.1)-(3.3) & (4.1) yields the following expression for the total circular velocity

$$V_{c,\mathrm{tot}}^2 = \frac{GM_1 R^2}{\left(R^2 + (a_1 + b_1)^2\right)^{3/2}} + \frac{GM_2 R^2}{\left(R^2 + (a_2 + b_2)^2\right)^{3/2}} + \frac{v_0^2 R^2}{R_c^2 + R^2}. \qquad (4.2)$$

Within Eq. (4.2) lies a hand-full of parameters that need to be determined. They are M_1, M_2, v_0, a_1, a_2, b_1, b_2 and R_c. The next task becomes determining these parameters.

4.1   Determining the parameters

The circular velocity of an object is not a direct observable in nature. It is for this reason we need to convert the modeled circular velocity into components which we could compare to observational data. If we imagine observing a maser for example, two things that are possible to observe are its radial velocity and its proper motion. In the model, such observables become the radial and tangential velocity, respectively. The comparable velocity components are illustrated in Figure 4.1.
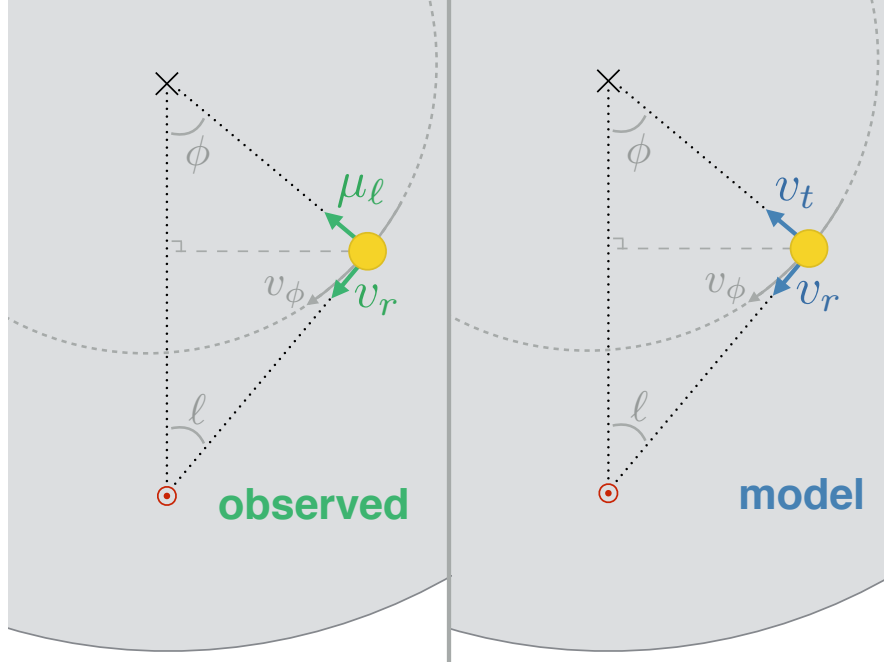
Figure 4.1: Plan view of the Galaxy. Here, v_ϕ represents the circular velocity. The red dotted circle represents the Sun, the black cross represents the Galactic center and the yellow circle represents a point source of light. Left frame shows the observable velocity components: the proper motion in direction of longitude, μ_ℓ, and the radial velocity, v_r. Right frame shows the modeled velocity components: the tangential velocity, v_t, and the radial velocity, v_r.

The principle way to determine the parameters in Eq. (4.2) is so check for which set of those parameters the modeled radial and tangential velocity components fit best with the corresponding velocity components from data. To find a best fitting model I use a combination of two techniques. The first is using the MCMC approach, which is explained in section 3.3, to search through the parameter space, finding the best-fitting model (after which we can even recover the mean value and a standard deviation for each sampled parameter). The second, is to put the probability used in the MCMC algorithm in terms of a Bayesian posterior, which is explained in section 3.2. Doing so allows me to take results from previous studies into account, so called priors, to further constrain the model. The full list of priors used can be seen in Table 4.1.

Table 4.1: All Bayesian priors that are used in order to constrain the models. M_1 is the total mass of the bulge. R_{bc} is the assumed radial extent of the bulge region. R_d is the disk scale length. $F_{z,1.1}$ is the vertical force an object would be subject to at 1.1 kpc from the disk at $R = R_0$ where R_0 is the distance from the Sun to the the Galactic center. $F_{R,50}$ is the radial equivalent at 50 kpc from the Galactic center. $\mu_{\mathrm{Sgr\,A^*}}$ is the proper motion for the Sun w.r.t. the Super-massive black hole (SgrA*) at the Galactic center.

Parameter	Value	Source
M_1	$(8.9 \pm 2) \times 10^9 \, M_\odot$	Bissantz & Gerhard (2002)
R_{bc}	2.5/3.5/4.0 kpc	Bland-Hawthorn & Gerhard (2016)
R_d	2.5 ± 0.4 kpc	Bland-Hawthorn & Gerhard (2016)
$F_{z,1.1}$	$2\pi G \times (71 \pm 6) \, M_\odot \, \mathrm{pc}^{-2}$	Kuijken & Gilmore (1991)
$F_{R,50}$	$G \times (2.16 \pm 0.4) \times 10^2 \, M_\odot \, \mathrm{pc}^{-2}$	Wilkinson & Evans (1999)
$\mu_{\mathrm{Sgr\,A^*}} \times R_0$	$239 \pm 9 \, \mathrm{km\,s}^{-1}$	Reid & Brunthaler (2004)

4.2 Data

The data used to constrain my model comes from two sources. The parallax, radial velocity and proper motion of maser sources and the radial velocity of HI gas. The components from these data sets and the corresponding modeled components are summarized in Table 4.2.

4.2.1 Maser data

The maser data used in this thesis work were obtained from Reid et al. (2014), which, in turn, obtained the data from the European Very-long-baseline interferometry (VLBI) Network, and the Japanese VLBI Exploration of Radio Astrometry project. As the names suggest, networks of ground-based radio telescopes have been used in sync to obtain accurate trigonometric parallaxes to the maser sources.

The 104 maser sources provided are given in Equatorial Coordinates (EC), which is a natural frame of reference for an observer. The observables are a, d, ϖ, σ_ϖ, μ_a, σ_{μ_a}, μ_d, σ_{μ_d}, v_r, σ_{v_r}. These are: right ascension (R.A.), declination (Dec.), parallax, error in parallax, proper motion in the direction of right ascension, its error, proper motion in the direction of right declination, its error, radial velocity and its error, respectively. The velocity components as obtained from the model and how they are transformed from one coordinate system to EC is shown in Appendix B.

4.2.2 HI emission data

The radial velocity data from the interstellar medium (ISM), as traced by HI emission lines, is used (Malhotra 1995). In reality, the gas does not have a singular uniform rotational velocity for a given Galactic longitude ℓ, as seen in Figure 4.2. That is why I use a simplified model, where only the maximum radial velocity at a given ℓ is considered. In the model, such a maximum is located where the line of sight (direction of longitude) is exactly perpendicular w.r.t the Galactic center. This is known as the terminal velocity and is illustrated in Figure 4.3.
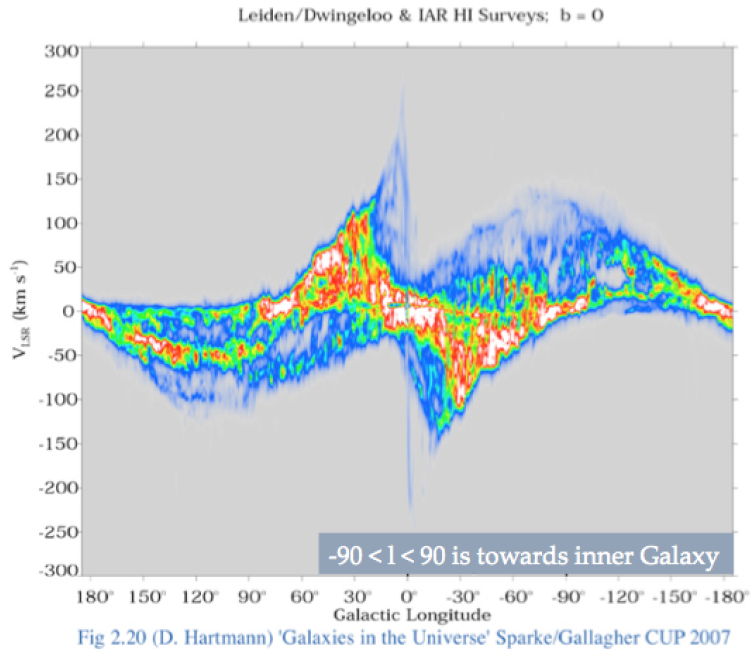
Figure 4.2: The radial velocity map of HI emission lines as a function of Galactic longitude, ℓ (Malhotra 1995).
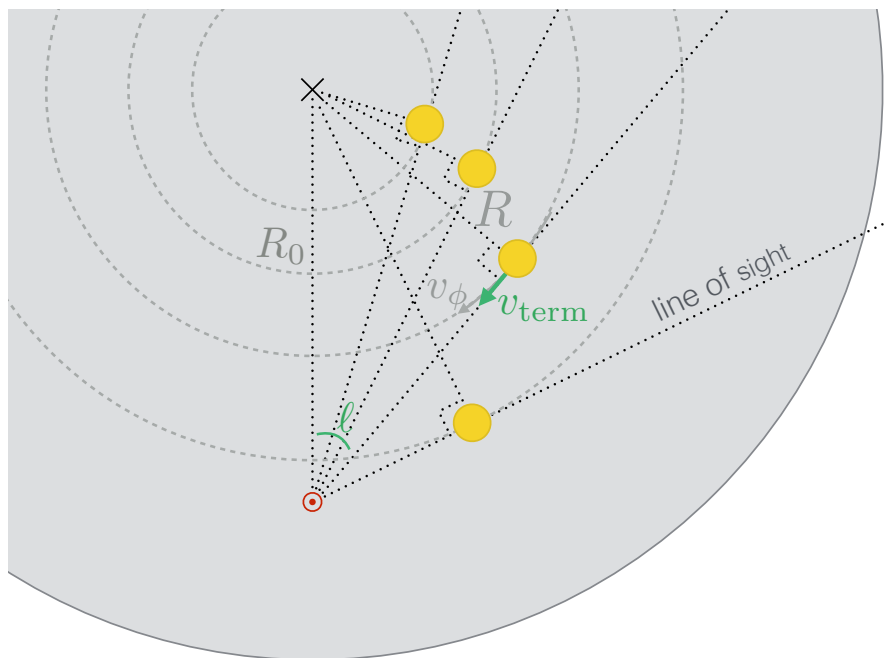

Figure 4.3: Plan view of the Galaxy in Heliocentric Galactic Polar coordinates (green). Here, $v_\phi = V_c$. The red circle represents the Sun, the black cross represents the Galactic center and the yellow circles represents HI emission line regions. The line of sight is perpendicular to the radius R.

The model for the terminal velocity, v_{term}, is obtained from Malhotra (1994)

$$v_{\text{term}} = \frac{|\sin\ell|}{\sin\ell}V_c(R_0\,|\sin\ell|) - (V_c(R_0) + V_\odot)\sin\ell, \tag{4.3}$$

where $V_\odot$ is the Sun's peculiar velocity in Galactocentric y-direction w.r.t. the velocity of a hypothetical star at solar position in circular orbit ($V_\odot = -12.24\,\text{km s}^{-1}$, McMillan (2011)), ℓ is the Galactic longitude and R_0 is the distance from the Sun to the GC. Thus, for a given line of sight, i.e. ℓ, and given the constants $V_\odot$ and R_0, it is possible to recover the terminal velocity from the model, which can be compared to observations.

Table 4.2: Summery of the velocity components used to constrain the models.

Velocity component	Observable	Modeled
Proper motion in R.A.	μ_a^o	$v_{t,a}^m \varpi^m$
Proper motion in Dec.	μ_d^o	$v_{t,d}^m \varpi^m$
Radial velocity	v_r^o	v_r^m
Terminal velocity	v_{term}^o	v_{term}^m

4.3 Comparing the model to data

Now that we have models which can reproduce predicted observables it is time to derive a best-fitting model. In section 3.2 I introduced the likelihood but did not properly define it.

Parameters, as obtained either from observation or models, come with errors. In nature, however, there should be a platonic, 'true' value for a physical parameter. The pdf thus needs to be evaluated against true values. For this reason, the probability P, which is the likelihood in the Bayesian posterior, takes on the form

$$P(\theta_o|\theta_m) = \int_0^\infty P_G(\theta_o|\theta_t)P_G(\theta_t|\theta_m)\,\mathrm{d}\theta_t, \tag{4.4}$$

where θ_t are the true values and the subscript $_o$ represents the observed value. This construction can be visualized as illustrated in Figure 4.4.

The general solution for Eq. (4.4), which now includes errors from both the observations and the models, is

$$\boxed{P(\theta_o|\theta_m) = \frac{\beta}{\sigma_o\sigma_m\sqrt{2\pi}}\text{Exp}\left[\frac{\alpha^2}{\beta^2} - \zeta\right],} \tag{4.5}$$

$$\frac{\left(\sigma_m^2\theta_o + \sigma_o^2\theta_m\right)^2}{\left(\sigma_m^2 + \sigma_o^2\right)^2} = \alpha^2\,; \qquad \frac{\sigma_m^2 + \sigma_o^2}{2\sigma_o^2\sigma_m^2} = \frac{1}{\beta^2}\,; \qquad \frac{\sigma_m^2\theta_o^2 + \sigma_o^2\theta_m^2}{2\sigma_o^2\sigma_m^2} = \zeta. \tag{4.6}$$

The full derivation that takes you from Eq. (4.4) to Eq. (4.5) is shown in Appendix A. Note that Eq. (4.5) is independent of any true parameter.
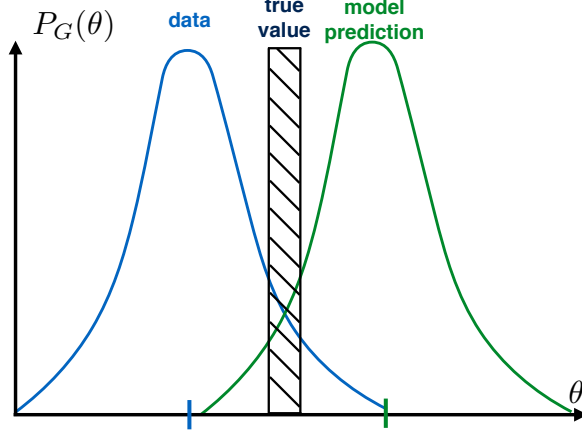
Figure 4.4: The dashed box represents the sharply peaked pdf of a true value. The two Gaussian pdfs represent the observed (blue) and modeled (green) location of the parameter. In a perfect world, all of these peaks would align on a single 'true' value.

The formulation of Eq. (4.5) has also introduced something significant which is an error term in the model, namely σ_m. This is akin to introducing a perturbation to an otherwise perfectly circular orbit. σ_m is set to $7\,\mathrm{km\,s^{-1}}$ because this is the estimated random velocity for an object residing in a spiral arm (McMillan 2011). This means that, for whatever velocity component is being evaluated with the probability P, it is now being treated as being on a near-circular orbit.

The Bayesian posterior can now be calculated by multiplying the likelihoods (listed in Table 4.2) and the priors (listed in Table 4.1) together

$$
\begin{aligned}
\text{posterior} = &\left(\prod_{i=1}^{N_{\mathrm{m}}} P(\mu_{a,i}^o|\mu_{a,i}^m) \times P(\mu_{d,i}^o|\mu_{d,i}^m) \times P(v_{r,i}^p|v_{r,i}^m)\right) \times \left(\prod_{i=1}^{N_{\mathrm{t}}} P_G(v_{\mathrm{term},i}^o|v_{\mathrm{term},i}^m)\right) \times \\
&P_G(\varpi^o|\varpi^m) \times P_G(a_1^o|a_1) \times P_G(b_1^o|b_1) \times P_G(M_1^o|M_1) \times \\
&P_G(F_{R,50}^o|F_{R,50}^m) \times P_G(F_{z,1.1}^o|F_{z,1.1}^m) \times P_G(\mu_{\mathrm{Sgr\,A^*}}^o|\mu_{\mathrm{Sgr\,A^*}}^m),
\end{aligned}
$$

(4.7)

where N_m is the number of masers and N_t is the number of terminal velocities from the HI data. The lack of a superscript for the variables in the second argument in P_G in the second row in Eq. (4.7) means that these are test variables in the MCMC algorithm. It should be reemphasized that the probability terms P have a built in error in the model but the terms P_G do not. So the error terms are not applied to the priors or the terminal velocity (because the observational errors are as low as $\sim 2\,\mathrm{km\,s^{-1}}$ (Malhotra 1995), which, compared to the error introduced in the model $\sim 7\,\mathrm{km\,s^{-1}}$, is negligible).

4.4 Spiral perturbation

There is no complete understanding of the origin and evolution of spiral phenomena. There is therefore neither a universal model or modeling technique whose results correctly predict the

long-term evolution of the majority of galactic systems. Developments of different theories have been made and the most common ones do solve some systems in some situations.

A common and classical way of modeling the spiral perturbations for a galactic system, that is also simple and analytic, is to regard the perturbations as static, non-material and traveling density waves. Quasi-stationary density wave theory is commonly associated with Grand Design galaxies, which are galaxies with prominent and well-defined spiral arms. In this regime, the arms are long-lived and rotate with fixed pattern speed. As mentioned in section 2.2, the framework for such a model has in part been developed by Lin & Shu (1964).

In numerical simulations, however, it is typical to see systems that do not remain static but develop transient spiral arms (Semczuk et al. 2017). Such results motivate the use of dynamical spiral models to which there are a few popular ones. The swing amplification model finds that given a differentially rotating disk, a leading and trailing density pattern emerges from the disk's shear. From here, spiral arms are created as wave modes eventually meet and amplify due to self-gravity (Dobbs & Baba 2014). The tidal interactions model is good at making grand design galaxies by introducing tidal interaction from surrounding systems. The bar driven spirals model works to produce spirals as a byproduct of gravitational field generated by a rotating strong (usually) bar. Even models where DM is the driving force are explored.

In light of the wide use of axisymmetric models of the MW among the community and the complexity levels that come with numerical simulations, the model deployed in this thesis work is inspired by the static wave equation. The parametric solutions that were used are obtained from Bobylev & Bajkova (2014), where the velocity perturbations in radial and azimuthal direction, $V_R = f_R \cos\chi$ and $\Delta V_\phi = f_\phi \sin\chi$, respectively, are given. Here, f represents the amplitude of the wave and χ represents the radial phase of the wave. Given that i represents the spiral pitch angle, a parameter that determines the amount of winding the spiral pattern has, and m represents the number of spiral arms in the system, the radial phase of an arm is given by

$$\chi = m \left[\cot(i) \ln(R/R_0) + \theta\right] - \chi_\odot \tag{4.8}$$

where $\chi_\odot$ is the correction for the radial phase of the Sun and θ is a stars position angle measured in the direction of Galactic rotation.

In effect, we are moving from a system of near-circular orbit

$$(v_R, v_\phi, v_z) = (\ 0,\ V_c(R),\ 0\ ), \tag{4.9}$$

to a system perturbed by spiral structure

$$(v_R, v_\phi, v_z) = (\ V_{R,\mathrm{sp}}(R,\phi),\ V_c(R) + \Delta V_{\phi,\mathrm{sp}}(R,\phi),\ 0\ ). \tag{4.10}$$

Models with 2 and 4 arms will be tested.

Chapter 5

Results

The method presented in this thesis results in Bayesian probability distribution functions sampled by an MCMC chain for a set of parameters describing axisymmetric models of the MW and models of static wave-like spiral perturbations all of which can be seen in sections 5.3, 5.4, 5.5, 5.6, 5.7. We also determined a best fitting model in each case which are shown in sections 5.1 and 5.2. Since the models contain many parameters or priors that can be changed, I test a few different scenarios. Each section will therefore showcase a model for a Galaxy with two spiral arms and one for four spiral arms.

The resulting azimuthal and radial velocity distribution for the best-fitting spiral arm model is shown in section 5.1. In the same section, I show the residual velocity vectors, comparing the the best-fitting axisymmetric and spiral arm model to the observed values of the masers. The best fitting model for the terminal velocity is shown in section 5.2. The vertical and radial force are shown in section 5.3. Sections 5.4, 5.5, 5.6 and 5.7 show the sets of parameters used to produce the above results and are shown as histograms which are obtained by binning accepted parameters in the MCMC algorithm.

5.1   Velocity maps

The left panels in Figures 5.1 (two-armed) and 5.2 (four-armed) show the best-fitting total (axisymmetric model + spiral arms, $V_\phi + \Delta V_{\phi,\mathrm{sp}}$) azimuthal velocity distribution and the right panels show the radial velocity distribution V_R. The azimuthal velocity perturbation for the two armed model is $\Delta V_{\phi,\mathrm{sp},2} \approx 15\,\mathrm{km\ s^{-1}}$ and for the four armed model $\Delta V_{\phi,\mathrm{sp},4} \approx 1\,\mathrm{km\ s^{-1}}$. The radial velocity perturbation for the two armed model is $\Delta V_{R,2} \approx 0.6\,\mathrm{km\ s^{-1}}$ and for the four armed model $\Delta V_{R,4} \approx 16\,\mathrm{km\ s^{-1}}$.

As a remark, because of the almost vanishing azimuthal velocity perturbation for the four armed model and the fact that the velocity towards the center of the Galaxy goes to $\approx 150\,\mathrm{km\ s^{-1}}$, I cut out any velocity that is not in the region $240\,\mathrm{km\ s^{-1}} < V_\phi < 250\,\mathrm{km\ s^{-1}}$ in Figure 5.2a. Otherwise, because of the plotting software's (MATLAB) color gradient scale functionality, the azimuthal spiral perturbation $\approx 2\,\mathrm{km\ s^{-1}}$ would never have been visible as the total azimuthal velocity is plotted and the tiny difference is hard to distinguish.

(a) Azimuthal velocity map.
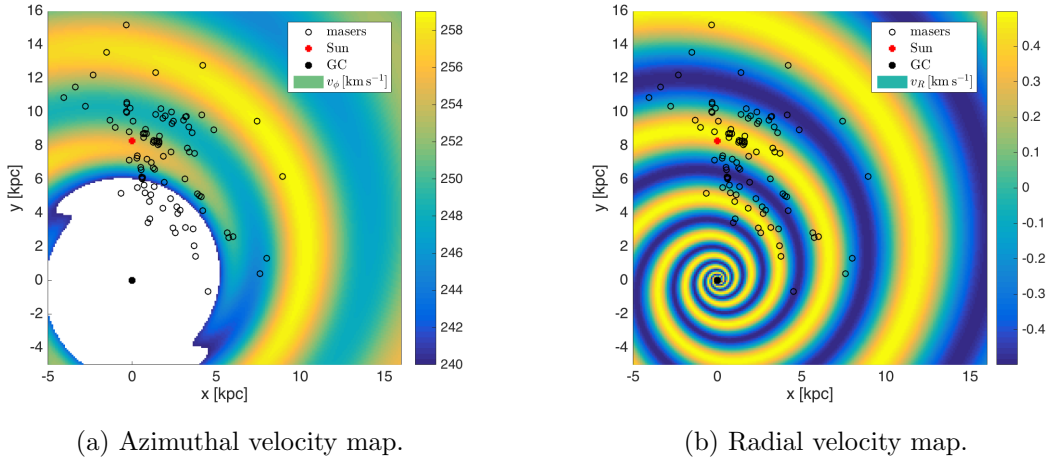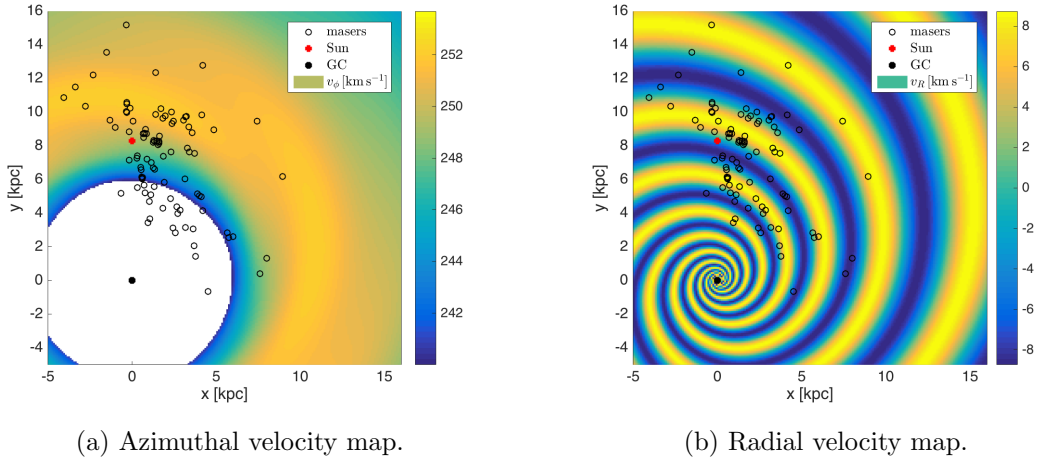
(b) Radial velocity map.

Figure 5.1: Velocity maps for the best-fitting parameters in the interval $-5 \leq x, y \leq 16$. Here, the spiral model has 2 arms and the bulge cut off radius $R_{\mathrm{bc}} = 3.5$ kpc.


(a) Azimuthal velocity map.

(b) Radial velocity map.

Figure 5.2: Velocity maps for the best-fitting parameters in the interval $-5 \leq x, y \leq 16$. Here, the spiral model has 4 arms and the bulge cut off radius $R_{\mathrm{bc}} = 3.5$ kpc.

Another way to visualize and to check the validity of the models is to subtract the modeled velocity components from that of the data. In other words, to show the residuals. Figures 5.3a and 5.3b show the face on view of the Galaxy where the velocity components of the axisymmetric model has been subtracted from that of the maser data and the axisymmetric model with spiral perturbations subtracted from the maser data, respectively. Figures 5.4a and 5.4b show the same for a four armed model. Finally, the residual between the axisymmetric model and the model including spiral perturbations is show in Figures 5.3c and 5.4c for a two armed and a four armed model respectively.

The scale of the velocity vectors on these plots should be noticed. The residuals on the top panels are scaled such that the length of the bottom left arrow corresponds to $200 \, \mathrm{km \, s^{-1}}$ and the bottom panels are scaled by $7 \, \mathrm{km \, s^{-1}}$. The latter is to highlight the residuals between the models as they are rather tiny.
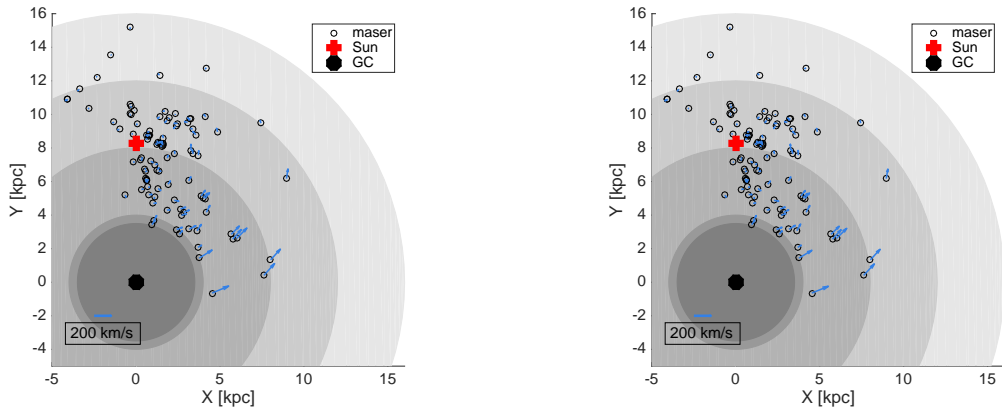
(a) Maser data versus axisymmetric model.

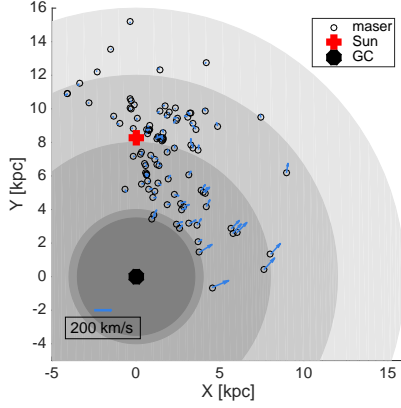(b) Maser data versus spiral perturbation model.
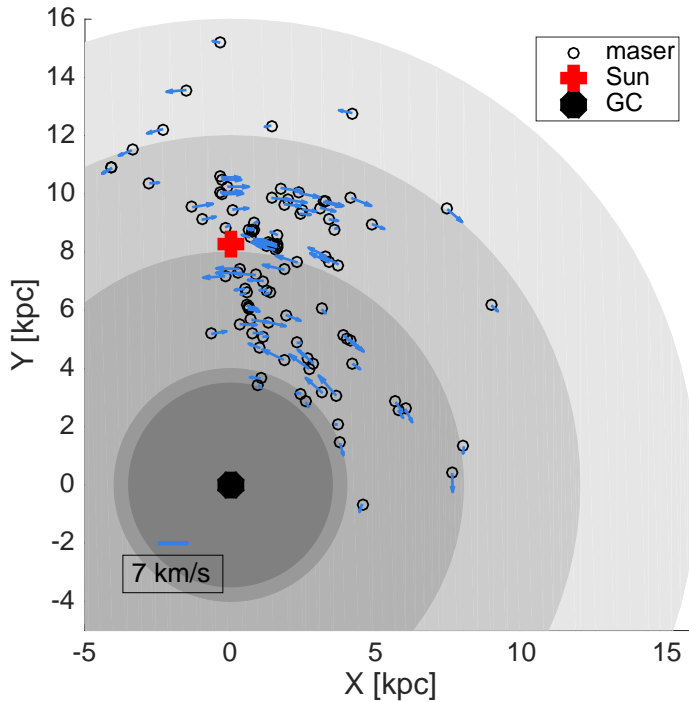
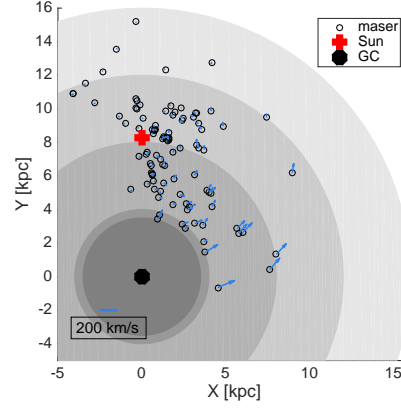(c) Axisymmetric model versus spiral perturbation model.

Figure 5.3: The residuals between the observed and modeled velocity components of masers. Data given by Reid et al. (2014). The gray scale is indicates 5 kpc radial increments except for the first one close to the Galactic center with indicates the bulge cut off radius. Here, the spiral model has 2 arms and the bulge cut off radius $R_{bc} = 3.5$ kpc.

Since the parallax becomes very small far away, the error in the measurements become very large which in turn make the estimate for the proper motion suffer. Because I am modeling the masers to be on near circular orbits, the velocity vectors will be perpendicular to a line that joins the source to the Galactic center. Combining the calculated velocity vectors from my model with the large errors for the masers far away results in the large residuals seen
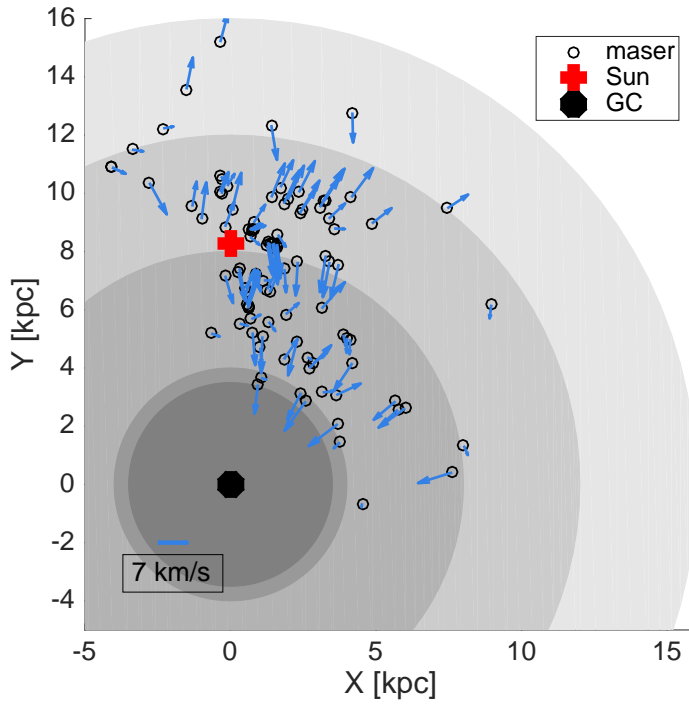
towards to bottom right corner in the plots.

(a) Maser data versus axisymmetric model.

(b) Maser data versus spiral perturbation model.

(c) Axisymmetric model versus spiral perturbation model.

Figure 5.4: The residuals between the observed and modeled velocity components of masers. Data given by Reid et al. (2014). The gray scale is indicates 5 kpc radial increments except for the first one close to the Galactic center with indicates the bulge cut off radius. Here, the spiral model has 4 arms and the bulge cut off radius $R_{\mathrm{bc}} = 3.5$ kpc.

5.2 Terminal velocity

The best fitting models for the terminal velocity curve as a function of Galactic longitude are shown in Figures 5.5 and 5.6 for a two armed and a four armed model respectively. The left panels show the full velocity distribution in $-90° < \ell < 0°$ and $0° < \ell < 90°$. The right panels zooms in on the $-90° < \ell < 0°$ region such that the deviations between the models can clearly be seen. It is clear from the two armed model (Figure 5.5b) that the model with the spiral perturbations follows the data better than the axisymmetric model.
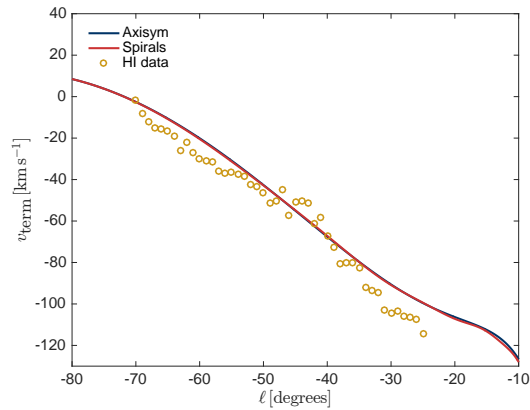

(a) Terminal velocity curves.   (b) Zoomed in terminal velocity curves.
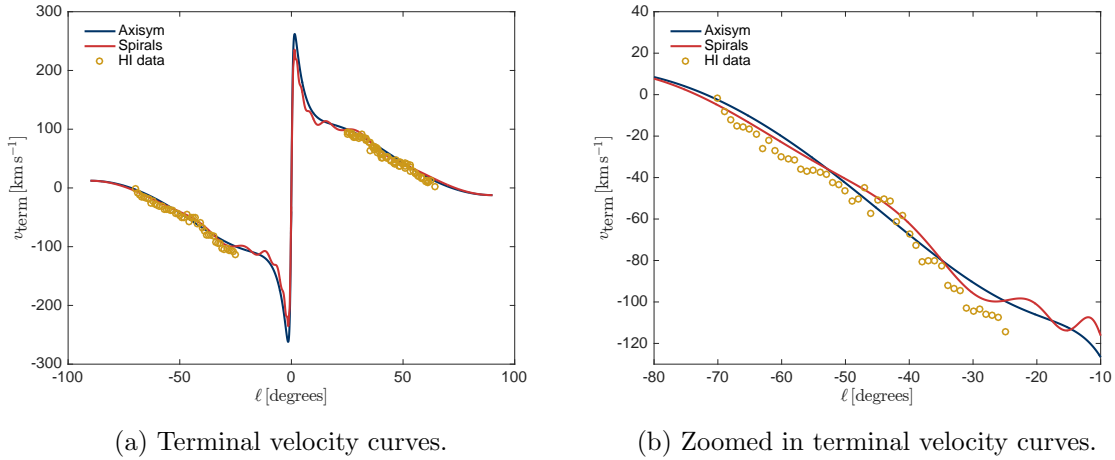
Figure 5.5: (a) shows the terminal velocity (line of sight velocity) of HI line emission as a function of Galactic longitude, ℓ. The lines represents the best-fit models, (blue: axisymmetric; red: spiral perturbation) and circles show the observed values Malhotra (1995). (b) shows a zoomed in version of (a) to better show the difference between the models. Here, the spiral model has 2 arms and the bulge cut off radius $R_{bc} = 3.5$ kpc.
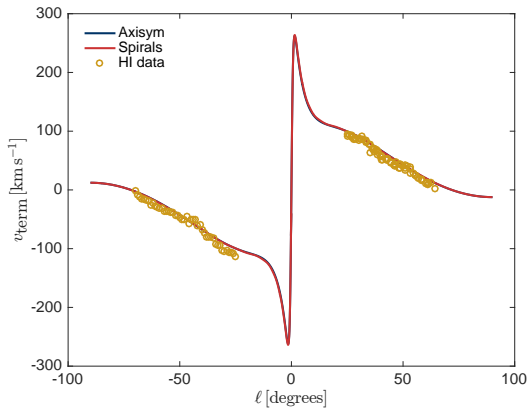
(a) Terminal velocity curves.

(b) Zoomed in terminal velocity curves.

Figure 5.6: (a) shows the terminal velocity (line of sight velocity) of HI line emission as a function of Galactic longitude, ℓ. The lines represents the best-fit models, (blue: axisymmetric; red: spiral perturbation) and circles show the observed values Malhotra (1995). (b) shows a zoomed in version of (a) to better show the difference between the models. Here, the spiral model has 4 arms and the bulge cut off radius $R_{\mathrm{bc}} = 3.5$ kpc.

5.3 Radial and vertical force

Figures 5.7a and 5.8a show the histograms of the vertical force at solar distance and 1.1 kpc above the plane. Both models (axisymmetric and spiral) seem to agree with prior as determined by Kuijken & Gilmore (1991). This should not come as a surprise as my models and data sets are all in the plane.

Figures 5.7b and 5.8b show how the histograms of the radial force in the plane at 50 kpc from the Galactic center. Both the two armed and the four armed model show significant departures from the prior given by Wilkinson & Evans (1999). This is probably due to the the fact that the MN disk scale length a_2 also prefers a different value as compared to its prior as seen in Figures 5.11a and 5.12a since a_2 and F_R are parameters affected the radial extent of the disk.

(a) Vertical force $F_{z=1.1\,\mathrm{kpc}}$.

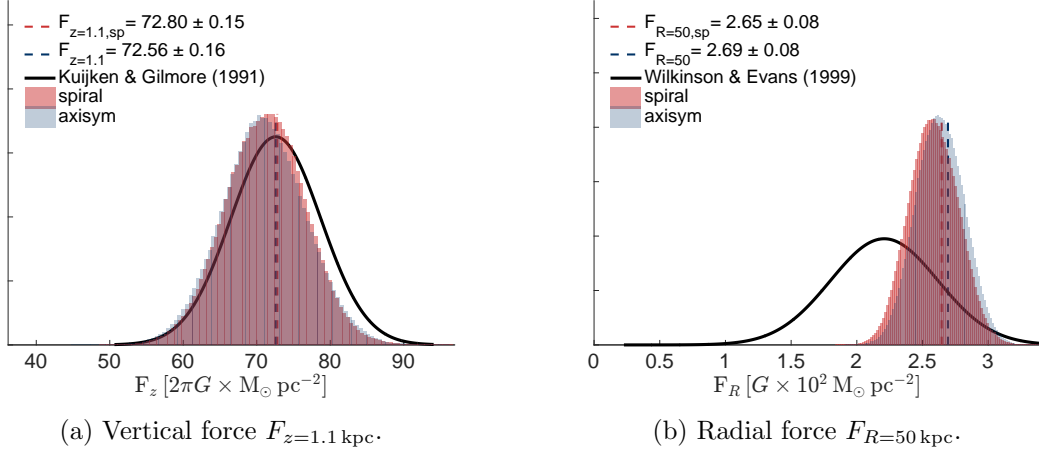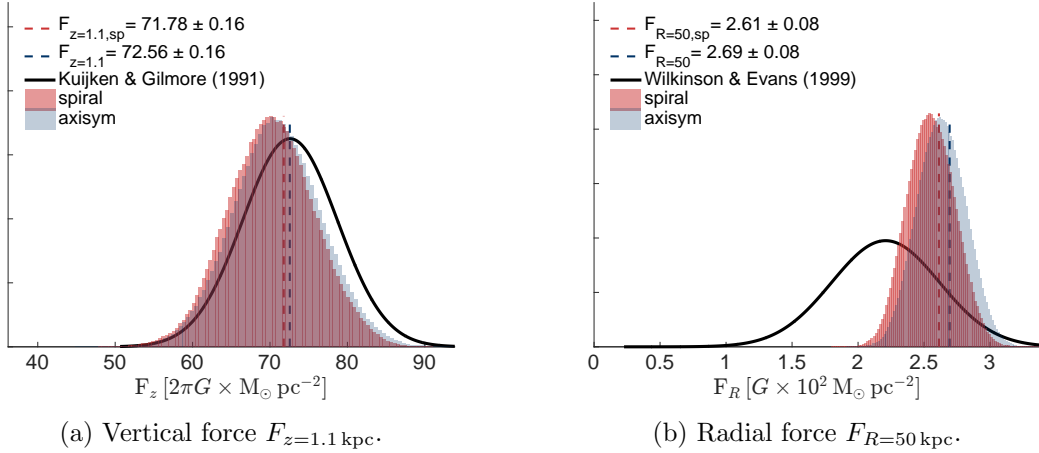(b) Radial force $F_{R=50\,\mathrm{kpc}}$.

Figure 5.7: Histogram showing (left) the vertical force per unit mass an object in the Galaxy would be subject to at $R = R_0$ and $z = 1.1$ kpc above the plane and (right) the radial force an object in the Galaxy would be subject to at $R = 50$ kpc and $z = 0$. Solid line shows estimates by Kuijken & Gilmore (1991) and Wilkinson & Evans (1999) respectively. The dashed line indicates the expectation value. Red histograms represents the spiral arm model and blue the axisymmetric model. Here, the spiral model has 2 arms and the bulge cut off radius $R_{\mathrm{bc}} = 3.5$ kpc.

(a) Vertical force $F_{z=1.1\,\mathrm{kpc}}$.

(b) Radial force $F_{R=50\,\mathrm{kpc}}$.

Figure 5.8: Histogram showing (left) the vertical force per unit mass an object in the Galaxy would be subject to at $R = R_0$ and $z = 1.1$ kpc above the plane and (right) the radial force an object in the Galaxy would be subject to at $R = 50$ kpc and $z = 0$. Solid line shows estimates by Kuijken & Gilmore (1991) and Wilkinson & Evans (1999) respectively. The dashed line indicates the expectation value. Red histograms represents the spiral arm model and blue the axisymmetric model. Here, the spiral model has 4 arms and the bulge cut off radius $R_{\mathrm{bc}} = 3.5$ kpc.

5.4 Bulge parameters

The bulge was the most heavily constrained part of the model. There were priors for both a_1 and b_2 as explained in section 3.2.1 (more detailed in Appendix C.2) and for the mass M_1. The resulting MN scale lengths and heights can be seen in panels (a) and (b) respectively in Figures 5.9 and 5.10. Because there were no data points in the bulge region or any other priors on the bulge, the a_1 and b_1 priors pretty much exactly outline the accepted MCMC values.

The mass, however, looks like a different story, as seen in Figures 5.9c and 5.10c. Both of them deviate from the prior but more interestingly, for the two armed model, the axisymmetric versus the spiral model strongly deviate from each other.
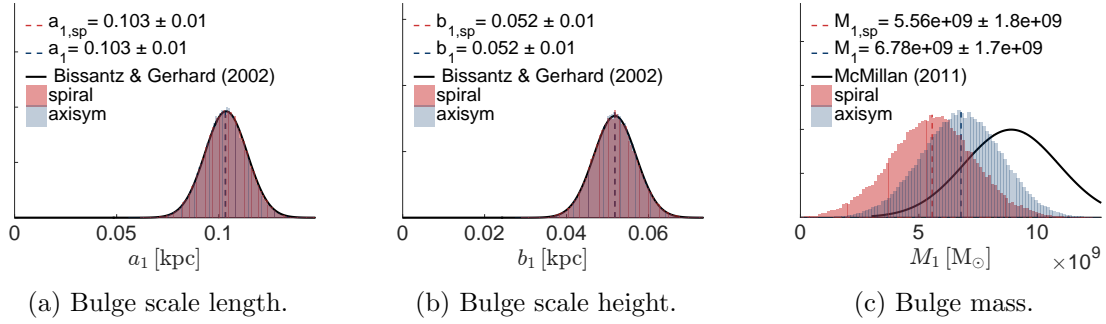

(a) Bulge scale length.   (b) Bulge scale height.   (c) Bulge mass.

Figure 5.9: Histograms of the axisymmetric spheroidal bulge with MN scale length a_1, scale height b_1 and mass M_1 with and without spiral perturbations (red and blue respectively). The dashed line indicates the expectation value. Here, the spiral model has 2 arms and the bulge cut off radius $R_{bc} = 3.5$ kpc. The solid lines represent the priors listed in table 4.1.
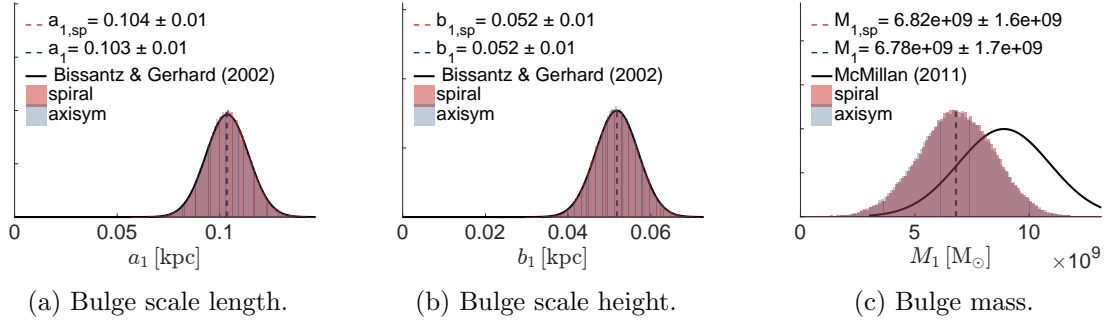

(a) Bulge scale length.   (b) Bulge scale height.   (c) Bulge mass.

Figure 5.10: Histograms of the axisymmetric spheroidal bulge with MN scale length a_1, scale height b_1 and mass M_1 with and without spiral perturbations (red and blue respectively). The dashed line indicates the expectation value. Here, the spiral model has 4 arms and the bulge cut off radius $R_{bc} = 3.5$ kpc. The solid lines represent the priors listed in table 4.1.

5.5   Disk parameters

Panels (a) and (b) show the MN scale length and heights respectively in Figures 5.11 and 5.12. The spiral model does not seem to change the values of a_2 and b_2 by any significance. However, both the two and the four armed models strongly deviate from the prior, which was given by the constructed relation between the MN scale length a_2 and the exponential disk scale length R_d as explained in Appendix C.1.

Again, as the mass of the bulge for a two armed model, the mass of the disk, M_2, as seen in Figure 5.11c, prefers different values depending on the different models.
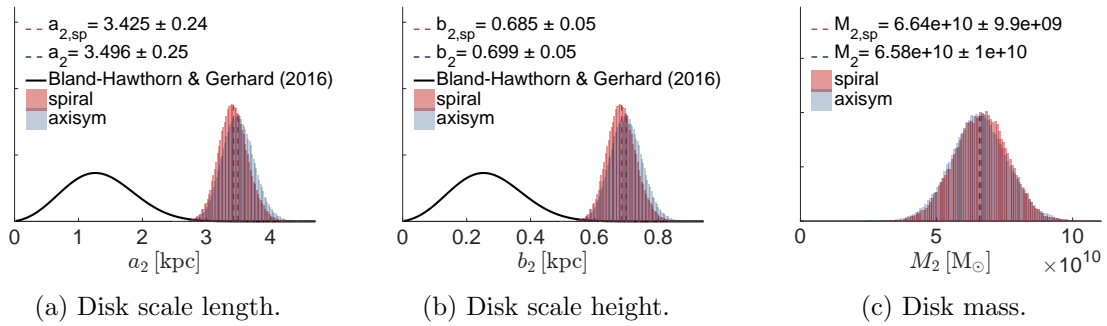

(a) Disk scale length.   (b) Disk scale height.   (c) Disk mass.

Figure 5.11: Histograms of the axisymmetric spheroidal disk with MN scale length a_2, scale height b_2 and mass M_2 with and without spiral perturbations (red and blue respectively). The dashed line indicates the expectation value. Here, the spiral model has 2 arms and the bulge cut off radius $R_{\rm bc} = 3.5$ kpc. The solid lines represent the priors listed in table 4.1.
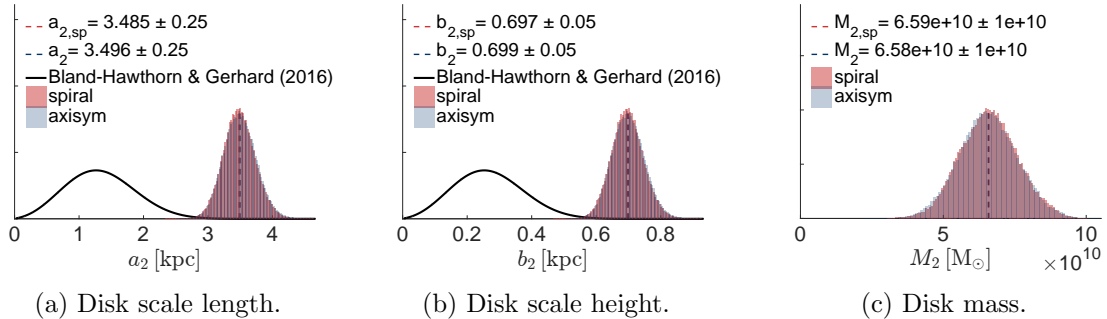

(a) Disk scale length.   (b) Disk scale height.   (c) Disk mass.

Figure 5.12: Histograms of the axisymmetric spheroidal disk with MN scale length a_2, scale height b_2 and mass M_2 with and without spiral perturbations (red and blue respectively). The dashed line indicates the expectation value. Here, the spiral model has 4 arms and the bulge cut off radius $R_{\rm bc} = 3.5$ kpc. The solid lines represent the priors listed in table 4.1.

5.6   Halo parameters

The top panels in Figures 5.13 and 5.14 show the resulting parameters from the logarithmic halo model. Shown in panel (a) is v_0, which is the maximum velocity in the logarithmic halo potential. It is clear that the different models (spiral versus non spiral) preferred different

values of v_0. Shown in panel (b) is the parameter governing the core radius of the halo. As this parameter has a wider pdf, the difference in mean values between the spiral and axisymmetric models are not considered significant.
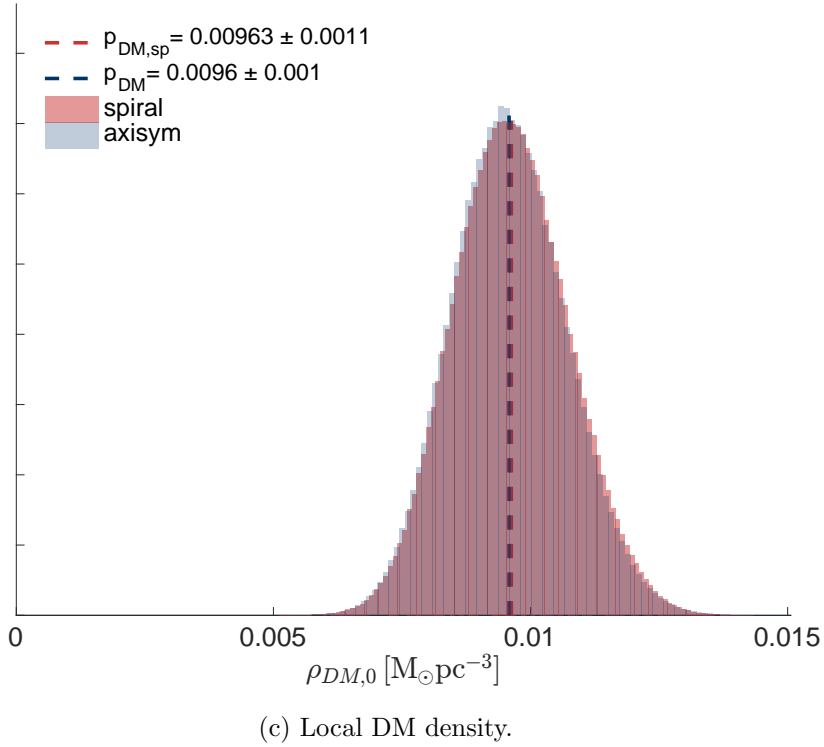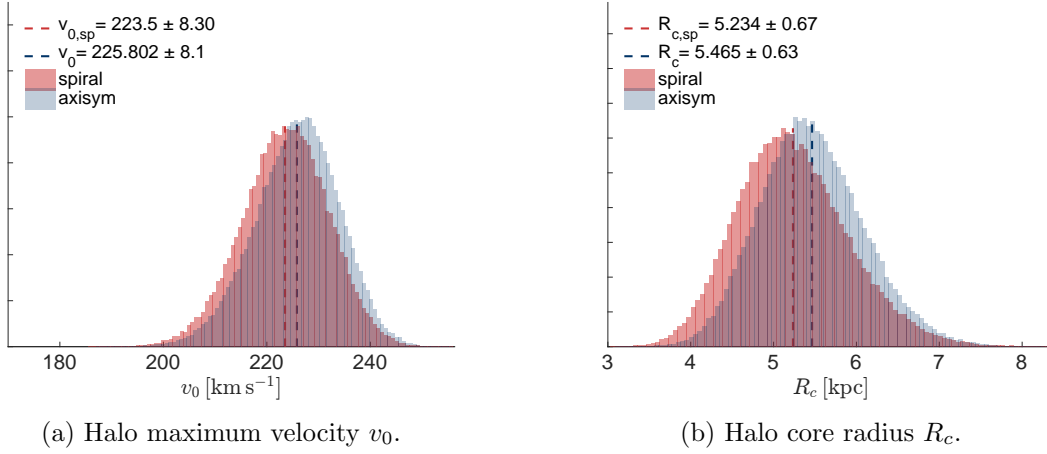

(a) Halo maximum velocity v_0.

(b) Halo core radius R_c.

(c) Local DM density.

Figure 5.13: Histogram of the logarithmic halo parameters v_0 (a), R_c (b) and (c) shows the local DM density. Red histograms represents the spiral arm model and blue the axisymmetric model. Here, the spiral model has 2 arms and the bulge cut off radius $R_{\mathrm{bc}} = 3.5$ kpc.

The resulting local DM density for the two armed model is $\rho_{\mathrm{DM},0} = 0.0096 \pm 0.001 \, M_\odot \, \mathrm{pc}^{-3}$ with a negligible model difference. For the four armed model, the difference is slightly more prominent where $\rho_{\mathrm{DM},0} = 0.0096 \pm 0.001 \, M_\odot \, \mathrm{pc}^{-3}$ for the axisymmetric models and $\rho_{\mathrm{DM},0} =$

$0.00917 \pm 0.001 \, M_\odot \, p^{-3}$ for the spiral arm models. These are however well within each others margins of error but should nevertheless be considered interesting.
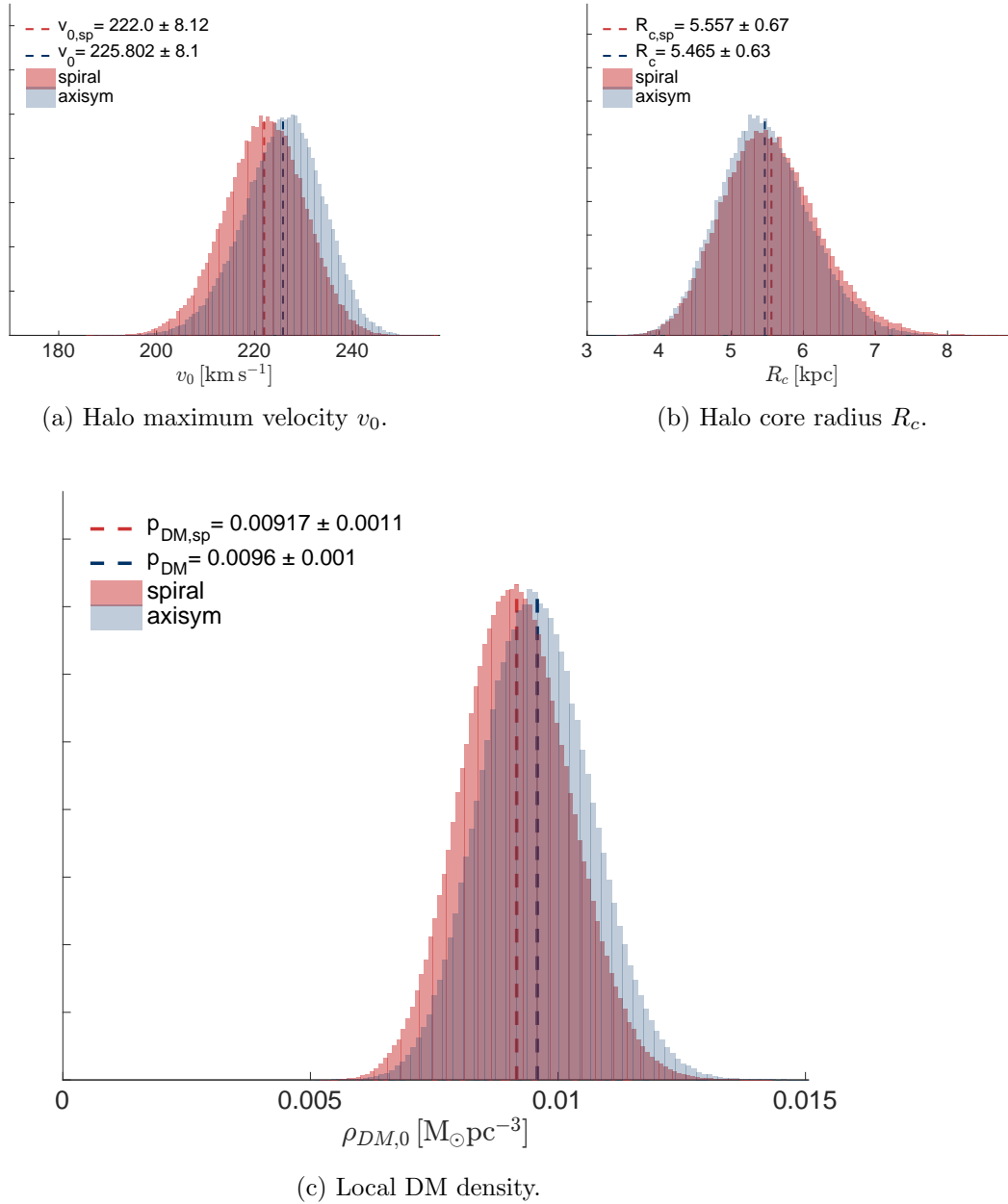

(a) Halo maximum velocity v_0.

(b) Halo core radius R_c.

(c) Local DM density.

Figure 5.14: Histogram of the logarithmic halo parameters v_0 (a), R_c (b) and (c) shows the local DM density. Red histograms represents the spiral arm model and blue the axisymmetric model. Here, the spiral model has 4 arms and the bulge cut off radius $R_{\mathrm{bc}} = 3.5$ kpc.

5.7 Spiral parameters

All of the spiral model parameters from Bobylev & Bajkova (2014) henceforth referred to as BB (section 4.4) are shown in Figures 5.15 and 5.16. Since these parameters govern the spiral structure, the resulting distribution of the two armed and the four armed parameters differ greatly.

The two armed model prefers a vanishing strength of the radial perturbation, $f_R \approx 0$ and an azimuthal perturbation strength $|f_\theta| >> 0$ as seen in Figures 5.15a and 5.15b respectively. Interestingly, the exact reverse is true for the four armed model. Here, $|f_R| >> 0$ and $f_\theta \approx 0$ as seen in Figures 5.16a and 5.16b. The two armed model also prefers a slightly smaller pitch angle than the four armed model as seen in Figures 5.15c and 5.16c. This could be explained geometrically as the four armed model basically needs more space or it would wind it self too tightly.
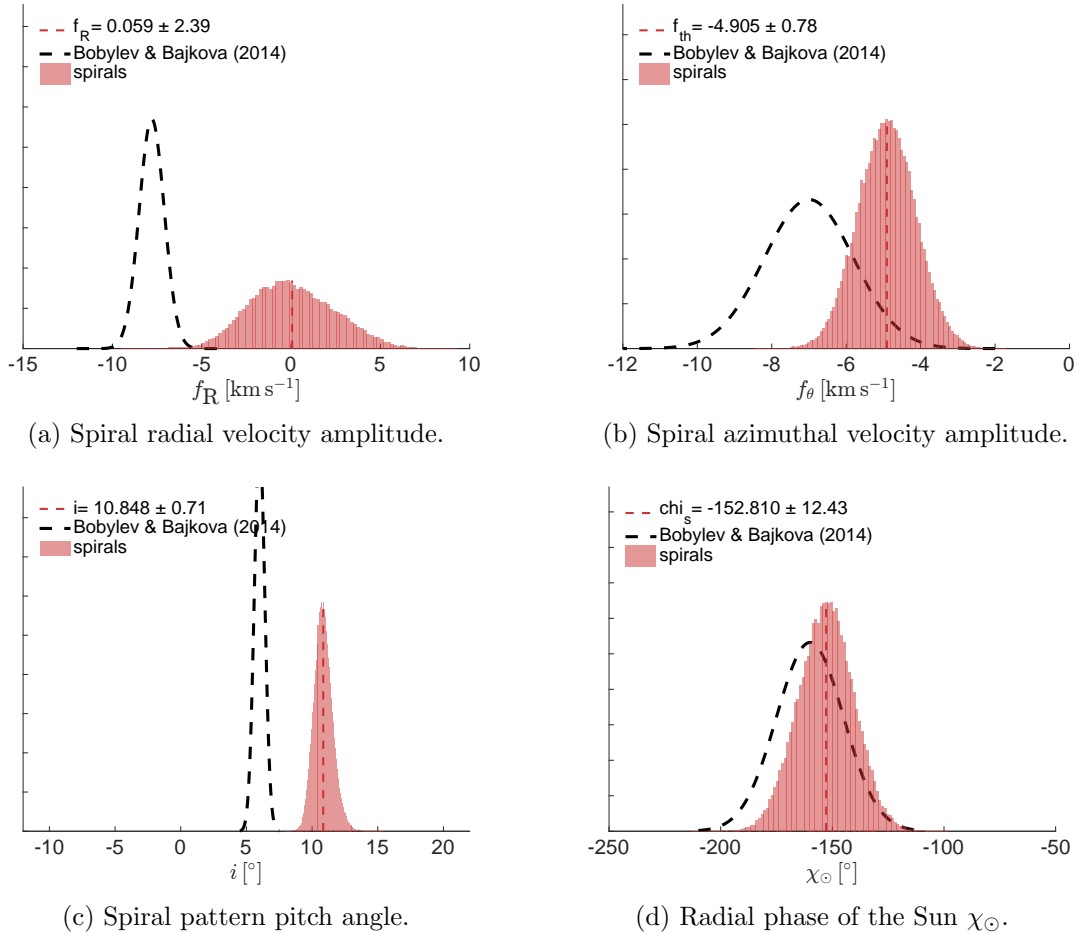

(a) Spiral radial velocity amplitude.

(b) Spiral azimuthal velocity amplitude.

(c) Spiral pattern pitch angle.

(d) Radial phase of the Sun $\chi_\odot$.

Figure 5.15: Histograms of the spiral perturbation parameters. (a) and (b) show the wave amplitude strengths for f_R and f_θ respectively. (c) and (d) show the wave pitch angle i and radial phase of the Sun $\chi_\odot$ respectively. Dashed lines represent results from Bobylev & Bajkova (2014) which used a 2 armed model. Here, the spiral model has 2 arms and the bulge cut off radius $R_{bc} = 3.5$ kpc.

A general comment to the discrepancy of my results to that of BB's (seen as dashed lines) is that BB used a different Galactic model that did not have a full model for the rotation curve. They also used a more narrow set of data compared to me, only a local sample of masers (within 1.5 kpc of the Sun) which also came from an older data set. As such, the deviations from my results are expected and in fact welcome as my results should be better.

Even though it would not be necessary, it is encouraging that the solar phase parameter, $\chi_\odot$, used in the two armed spiral model coincided well with BB's results as seen in Figure 5.15d as their model had two spiral arms.
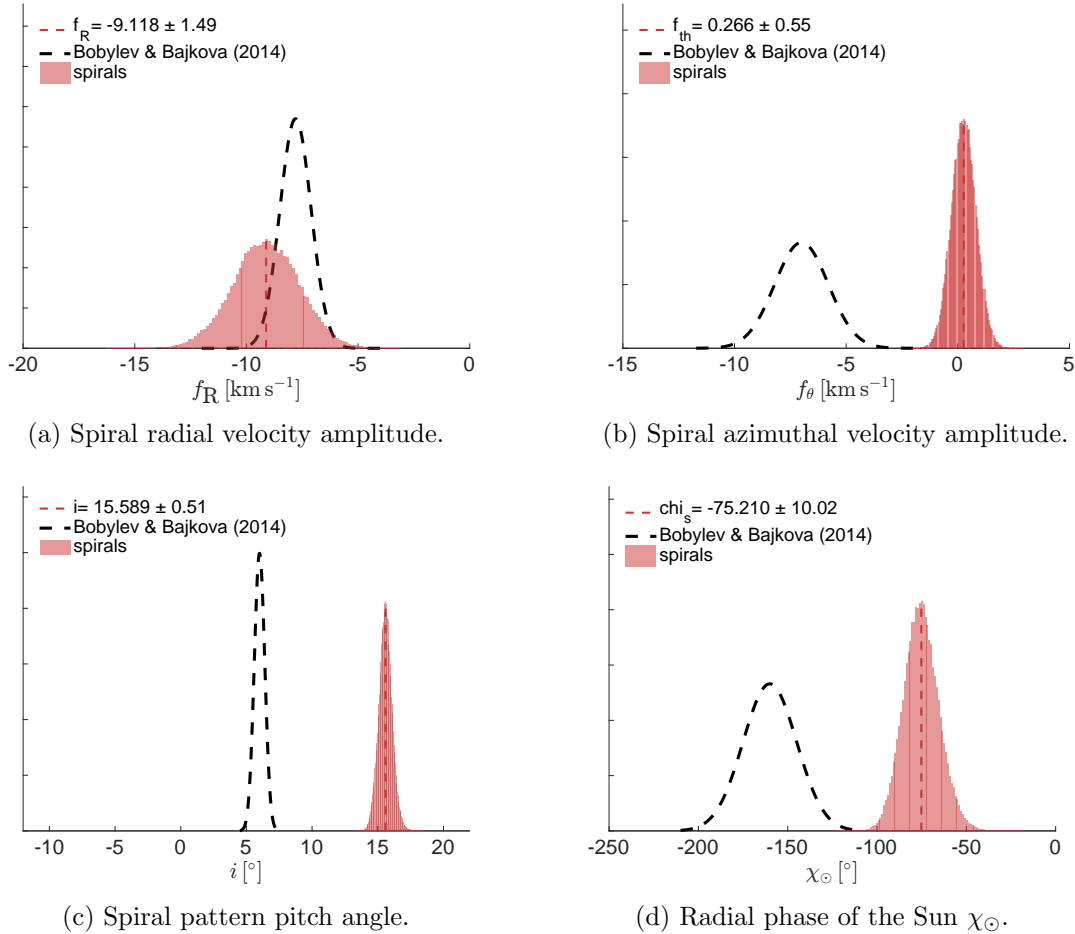

(a) Spiral radial velocity amplitude.

(b) Spiral azimuthal velocity amplitude.

(c) Spiral pattern pitch angle.

(d) Radial phase of the Sun $\chi_\odot$.

Figure 5.16: Histograms of the spiral perturbation parameters. (a) and (b) show the wave amplitude strengths for f_R and f_θ respectively. (c) and (d) show the wave pitch angle i and radial phase of the Sun $\chi_\odot$ respectively. Dashed lines represent results by Bobylev & Bajkova (2014) which used a 4 armed model. Here, the spiral model has 4 arms and the bulge cut off radius $R_{\mathrm{bc}} = 3.5$ kpc.

5.8   Robustness check

Since I have employed a statistical analysis which used a MCMC algorithm to find best-fitting parameters, it is useful to check whether or not choosing different initial trial parameters give

significantly different final results. I tested this by changing all of the initial conditions by $\pm 20\%$ and conclude that the final results seen in all the plots above does not change with any significance.

Furthermore, since the bulge cut parameter R_{bc} introduced in section 3.2.1 was chosen somewhat freely, although my choice for $R_{bc} = 3.5$ kpc was motivated by estimates from Bissantz & Gerhard (2002); Reid et al. (2014), the bulge region is still not well defined, I test different values for it. As such, I re-ran the code for six permutations of scenarios. For both a two and four armed model, I set R_{bc} to 2.0 kpc, 3.5 kpc and 4.0 kpc. It would be rather messy to show 4 additional sets of results so the most significant parameters that changed are shown in Tables 5.1 and 5.2 for a two and a four armed model respectively.

It should be noted that when I change R_{bc} in the model, I also change the region for which data points are accepted i.e. $R_{bc} = 2.0$ kpc will include more masers and terminal velocity points than $R_{bc} = 4.0$ kpc. In terms of accepted masers and accepted terminal velocity points, a bulge cut off radius of $R_{\mathrm{bc}} = 2.0$ kpc corresponds to 102/104 and 134/134 of accepted data points, $R_{\mathrm{bc}} = 3.5$ kpc corresponds to 101/104 and 115/134 and $R_{\mathrm{bc}} = 4.0$ kpc corresponds to 97/104 and 104/134.

Table 5.1: Varying the bulge cut off region R_{bc} for the two armed spiral model and showing the mean values for relevant parameters. When the mean values from an axisymmetric and spiral model differ by a meaningful amount I denote the value produced by the spiral model by (sp). A slot that is not labeled by (sp) means that the models produced a similar value.

R_{bc}	2.0 kpc	3.5 kpc	4.0 kpc
a_1/kpc	0.7	0.1	0.05
$M_1/10^{10}\,M_\odot$	1.2	0.55(sp)-0.67	0.7
a_2/kpc	3.3	3.5	3.3
$M_2/10^{10}\,M_\odot$	5.5	7(sp)-6.5	6.7(sp)-6.3
$\rho_{\mathrm{DM}}/M_\odot\mathrm{pc}^{-3}$	0.015(sp)-0.016	0.013(sp)-0.014	0.013(sp)-0.014
$f_R/\mathrm{km\ s}^{-1}$	*	0.0	-3.0
$f_\theta/\mathrm{km\ s}^{-1}$	-5.0	-5.0	-5.0
$v_{\mathrm{term,max}}/\mathrm{km\ s}^{-1}$	130	240	400

The $*$ in table 5.1 refers to a not well defined results. Here, the values for f_R spanned too large of a range. More specifically, f_R preffered values between the range $-3 < f_R/\mathrm{km\,s}^{-1} < 5$ and $7 < f_R/\mathrm{km\,s}^{-1} < 12$.

Table 5.2: Varying the bulge cut off region R_{bc} for the four armed spiral model and showing the mean values for relevant parameters. When the mean values from an axisymmetric and spiral model differ by a meaningful amount I denote the value produced by the spiral model by (sp). A slot that is not labeled by (sp) means that the models produced a similar value.

R_{bc}	2.0 kpc	3.5 kpc	4.0 kpc
a_1/kpc	0.7	0.1	0.05
$M_1/10^{10}\,M_\odot$	1.2	0.68	0.72
a_2/kpc	3.3	3.5	3.4
$M_2/10^{10}\,M_\odot$	5.1	6.6	6.5
$\rho_{\text{DM}}/M_\odot \text{pc}^{-3}$	0.016	0.013(sp)-0.014	0.014
$f_R/\text{km s}^{-1}$	-8.5	-9.1	-9.0
$f_\theta/\text{km s}^{-1}$	0.0	0.0	0.0
$v_{\text{term,max}}/\text{km s}^{-1}$	130	250	450

It is evident from Tables 5.1 and 5.2 that the bulge cut of radius R_{bc} does alter *some* of the parameters in a fairly significant way. The parameters that seem to be undisturbed and rather robust are the disk parameters (a_2 and M_2), the local DM density ($\rho_{\text{DM},0}$) and the spiral arm velocity strength parameters (f_R and f_θ) especially if the cut off at 2.0 kpc is omitted. The reason $R_{bc} = 2$ kpc differs from the rest can be understood by the fact that using masers close to the Galactic center allows a greater amount of statistical error both from the measurements and the poor modeling of the bulge region.

The bulge mass seems consistent with the afore mentioned arguments but the scale length a_1 is a different story. The resulting value of a_1 is heavily dependent on the chosen R_{bc}. Thankfully, as discussed above, the rest of the parameters are largely unchanged except for the rather extreme case of $R_{bc} = 2.0$ kpc.

The maximum terminal velocities, $v_{\text{term,max}}$ also differ greatly which that is directly coupled to the inconsistency of the bulge scale lengths. Critically, the good news is that the rest of the terminal velocity curves, beyond the bulge region, do not change at all, they still go through the data points just like in Figures 5.5b and 5.6b.

5.8.1 Adding exponential decay

In a further attempt to test different models and to try to resemble the MW structure to a greater accuracy, I add exponential terms to the spiral perturbations. This choice is motivated by the fact that observations reveal a exponential decaying disk as explained in section 2.1.2. The results that follow from this model are shown in Appendix D.

Chapter 6

Discussion & conclusion

The main goal of this thesis work is to show the effect of adding spiral perturbations to a commonly used axisymmetric model. Adding the simplest model for the spiral arms (i.e. an analytic wave equation) to one of the most commonly used and simple models for the Galactic structure (i.e. two axisymmetric disks with a logarithmic halo) results in slightly differently preferred parameters for the corresponding MW gravitational potential. However, these systematic differences are smaller than their corresponding statistical difference given my amount of data ($\sim$100 masers). As the amount of data increases, the statistical uncertainty will shrink (while there is no reason to expect that the systematic one will). Therefore studies of this kind will be increasingly important as the amount of data improves.

Adding spiral perturbations indicate that there could be, if further investigated upon and more data is added, a potentially more significant difference in local DM density. Such results are important for the scientific community as they look to constrain models of DM which effect dynamical modeling and simulations of the formation of the MW. Furthermore, the detectors build on earth that aim to detect scattering events between SM and DM particles rely on values for the local DM density as input for models of interaction rates. This should encourage further investigations.

For both the two armed and four armed model, the slight differences are visible when looking at the shifts in the mean values of the preferred model parameters which can be seen in (the two armed model) Figures 5.7, 5.9, 5.11, 5.13 and (four armed model) Figures 5.8, 5.10, 5.12, 5.14. One of the standout result in this thesis work is the importance of choosing the right number of spiral arms as they have polar opposite velocity configurations. The two armed model prefers a vanishing radial velocity perturbation but a non-vanishing azimuthal velocity perturbation $\Delta V_\phi \approx 16\,\mathrm{km\,s^{-1}}$. The opposite is true for the four armed model.

As one of the major challenges of this thesis work was to constrain the model with enough priors such that the the MCMC algorithm produced well-defined results, it is encouraging to see the resulting histograms taking on a Gaussian looking shape as seen in Figures 5.7 - 5.16. For example, in the early stages of this work, we assumed that the $F_z, F_R \,\&\, \mu_{\mathrm{Sgr\ A}^*}$ priors were enough to constrain the disk parameters. This turned out not to be the case and required putting efforts into finding a relation between the MN scale length (a_2) and some observational parameter. I claim that the developed relation between a_2 and R_d is unique to this thesis work. The full derivation of it can be found in Appendix C.1. This is also why

efforts were put into finding similar constraints for the bulge parameters. Otherwise, the now nice looking Gaussian histograms would look boxy and random where for example a_2 could wander from 0 to 8 kpc.

For the parameters in the spiral model (Figures 5.15 and 5.16) it is seen that the results from Bobylev & Bajkova (2014) (BB) differ significantly from my results. This is in part due to using a different model for the Galaxy than BB but also because of using newer and more inclusive data sets of masers. The aforementioned authors used a smaller and local sample, ≈ 30 and no farther than 1.5 kpc from the Sun. Their data set was provided by Xu et al. (2013), which aimed to investigate the local arm and used maser data mainly from Reid et al. (2009), as opposed to their updated list that I am using (Reid et al. 2014) with ≈ 70 additional maser sources at further distances.

One of the interesting results for the spiral parameters is the completely polar opposite choices of radial and azimuthal velocity strengths, f_R and f_θ, when it comes to a two versus a four armed spiral model as explained in section 5.7. This is an important result as they propagate to the resulting shape of the terminal velocity curves (Figures 5.5 and 5.6) and the velocity maps (Figures 5.1 and 5.2) for the models with different arms. The two armed model preferred a non-zero $|f_\theta|$ which translates into a non-zero $\Delta V_{\phi,\text{sp}}$. This explains the different shapes of the terminal velocity curves between the axisymmetric model, which depends on V_ϕ only, and the model with added spiral perturbation $V_\phi + \Delta V_{\phi,\text{sp}}$ as seen in Figure 5.5b. For the four armed model, however, $|f_\theta|$ is vanishing. This is why Figure 5.6b shows almost no discrepancy between the models for the terminal velocity. The same line of reasoning explains the difference between the radial and azimuthal velocity distributions as seen in Figures 5.1 and 5.2 when using a two or a four armed model.

It should be noted that the spiral model was not constrained by even a prior specific to the spiral parameters. It is encouraging that such unconstrained parameters are able to reproduce very similar results to BB for the two armed model as seen in Figure 5.15. The resulting well behaved values for all the spiral parameters shows the self-consistency of the methodology.

It could be tempting to imagine that adding any type of additional model to the axisymmetric model will result in shifted histograms. I therefore point to the residual plots shown in Figures 5.3 and 5.4 and argue that the top panels are in good agreement with each other. In other words, even though the typical residual (data vs model) is $\approx 20\,\text{km s}^{-1}$ near the Sun and increases to $\approx 200\,\text{km s}^{-1}$ towards the bottom right corner, the spiral model produces the same level of errors in roughly the same places. This is of course exactly what is highlighted in Figures 5.3c and 5.4c which shows the residuals between the models. The differences are of order less than the typical random velocity found in spiral arms $< 7\,\text{km s}^{-1}$ for the two armed model. For the four armed model, the differences between the models are slightly larger, creeping up to $\approx 7\,\text{km s}^{-1}$, which is still low.

The large errors seen in the bottom right corner as seen in the residual plots are simply due to the basic fact that these masers are far away and parallaxes are thus expected to be measured with greater uncertainty. Including these masers have definitely perturbed the results but to an unknown extent.

Most of the resulting parameters and fits seem to be consistent with previously determined values for the parameters and data. Both the axisymmetric and spiral model of the terminal velocity follows the HI data pretty well, especially the two armed spiral model. Even though

the disk scale lengths deviate a lot from their priors, they are consistent with Paczynski (1990). The resulting mass of the disk $M_2 = (6.5-7) \times 10^{10} \, M_\odot$ is also very close to the estimated value $M_2 = (4\pm1) \times 10^{10} \, M_\odot$. The resulting values of the vertical force is consistent with Kuijken & Gilmore (1991) and the resulting radial force slightly differs from that of (Wilkinson & Evans 1999), which are new results that I mostly owe to the newer data set. My resulting local DM density was $\rho_{\mathrm{DM}} = 0.0096 \pm 0.001 \, M_\odot \, \mathrm{pc}^{-3}$ for all models except for the four armed spiral model for which $\rho_{\mathrm{DM}} = 0.00917 \pm 0.001 \, M_\odot \, \mathrm{pc}^{-3}$. These values are within the confines fo the estimated $\rho_{\mathrm{DM}} = 0.006 - 0.020 \, M_\odot \mathrm{pc}^{-3}$ (McMillan 2011; Bovy & Tremaine 2012; Garbari et al. 2012; Zhang et al. 2013; Bovy & Rix 2013; Salucci et al. 2010). At solar radius, the resulting azimuthal velocity maps show consistent results $V_\phi \approx 240 \, \mathrm{km \, s}^{-1}$ compares to the estimated solar circular velocity inferred by the apparent proper motion of Sagittarius A*, $V_{c,\odot} = 239 \pm 9 \, \mathrm{km \, s}^{-1}$. For a two armed model, my resulting spiral parameters are generally consistent with those found by BB. Our results disagree mainly by choice of maser sources and modeling. They chose close by sources from an older data set and my masers spanned a larger range from a newer data set. The resulting pitch angles $i_{2\,\mathrm{arms}} = 10.9 \pm 0.7°$ and $i_{4\,\mathrm{arms}} = 15.6 \pm 0.5°$ are both in an accepted range for this still very debated parameter (Vallée 2015).

However, the preferred mass of the bulge is not consistent with estimates $1.4 - 1.8 \times 10^{10} M_\odot$ by Bland-Hawthorn & Gerhard (2016) which is double the mass predicted by my modeling. The bulge scale length is at least consistent with Paczynski (1990).

Authors that have used similar approaches as to mine, Bayesian statistics with forward modeling, omit spiral structure when for example determining mass models of the MW (Dehnen & Binney 1998; McMillan 2011). Bovy & Rix (2013) even did full dynamical modeling of $\sim 16,000$ G dwarf stars to fit that to their 3D action-based distribution function and a MW model with a halo, bulge, stellar and gaseous disk. No spiral arms! Here they derive parameters such as local surface density and the radial profile of the dark halo. Since they use a rather large sample (16,000 stars), their statistical errors are smaller. I therefore argue that systematic effects from including spirals could represent a significant fraction of the uncertainty of their work.

Bovy & Tremaine (2012) debunked a claim of a newly estimated local DM density that differed by an order of magnitude (Moni Bidin et al. 2012). In doing so, they used the same data as Moni Bidin et al. and claim to have found the latest most robust result $\rho_{\mathrm{DM}} = 0.008 \pm 0.003 \, M_\odot \mathrm{pc}^{-3}$. However, this estimate came from assuming a flat rotation curve, where the main argument seems to be that the local MW's rotation curve is pretty much flat (Xue et al. 2008; Fuchs et al. 2009). Again, as I have shown, this uncertainty could be underestimated because they have not considered the spiral perturbations. After all, the local DM density could differ by $\sim 0.001 \, M_\odot \mathrm{pc}^{-3}$ by including simplistic and unconstrained models for the spiral perturbations. There is a potential for Bovy & Tremaine (2012) to possibly improve on their results.

Another group that can benefit from my conclusions about the change in local DM density using spiral modeling is Piffl et al. (2014), which used $\sim 200,000$ giant stars from the RAdial Velocity Experiment (RAVE) within 1.5 kpc of the plane to estimate the local mass density and the shape of the DM halo. They find a larger mass of the DM halo than predicted by DM only simulations but an agreement with simulations including baryons. More importantly, one of their key results is an estimate for the local DM density and the shape of the halo. They find $\rho_{\mathrm{DM},0} = 0.0126 q^{0.89} \, M_\odot \mathrm{pc}^{-3}$ where $q \simeq 0.8$ once combined with literature results of

$\rho_{\mathrm{DM},0}$. As these authors are trying to answer big questions about the most massive structure in the MW which, when answered, inevitably leads to learning more about the rest of the Universe, it is important to consider the more detailed modeling of the MW, i.e. adding spiral structure to models.

6.1   Future outlook

If one is to continue arguing for the inclusion of spiral arms in models then what has been started in this thesis work needs to be continued and further built upon. From a modeling standpoint, even though the bulge region was not of major interest, if one is to make a fully consistent model of the MW, then the axisymmetric approximation need to be revised. Better alternatives of constraining the bulge region than used in this work should therefore be investigated.

There are of course other model improvements that one could make in order to get closer to reality. For instance, changing the Kuzmin surface density to that of the MN when constructing the relation between a_2 and R_d; or having a NFW DM density profile for the halo; or a bigger game changer, introduce a z component into the modeling. Unfortunately, this is tricky business because all of these implementations would force one to lose the simplicity and speed of the analytic modeling.

It would also be very interesting to se what happens when the masers on the far bottom right are excluded or any kind of different grouping of selection criteria. I suspect different results from the exclusion of those maser sources as their proper motions have very large error in parallax. More inclusion of errors are general in welcome since I have totally omitted error bars in my residual plots.

A major contribution is the wait for new data. The data set I used came from a group that is working on releasing a new data set with a few more multiples of the masers than I had. Furthermore, with Gaia releasing its data sets in the near future, the spiral structure should become more evident and models of spiral arms can be constrained.

Appendices

Appendix A

Allowing for error in the model

From Bayes' theorem we have the posterior

$$P(m|d) = \frac{P(d|m)P(m)}{P(d)}.$$

Imagining that we are interested in the 'true' (t) value of a velocity component v, we set up the equality where the posterior will be the product of two Gaussian pdfs G which both are being evaluated against the true parameter v_t (not to be confused with the 'tangential' velocity)

$$P(d|m) = \int_{-\infty}^{\infty} G(v_o|v_t)G(v_t|v_m)\,\mathrm{d}v_t$$

where $o = observation = data = d$.

$$P(d|m) = \frac{1}{2\pi\sigma_o\sigma_m} \int_{-\infty}^{\infty} \mathrm{Exp}\left[-\left(\frac{(v_o - v_t)^2}{2\sigma_o^2} + \frac{(v_t - v_m)^2}{2\sigma_m^2}\right)\right]\,\mathrm{d}v_t$$

$$P(d|m) = \frac{1}{2\pi\sigma_o\sigma_m} \int_{-\infty}^{\infty} \mathrm{Exp}\left[-\left(\frac{\sigma_m^2\,(v_o - v_t)^2 + \sigma_o^2\,(v_t - v_m)^2}{2\sigma_o^2\sigma_m^2}\right)\right]\,\mathrm{d}v_t$$

$$P(d|m) = \frac{1}{2\pi\sigma_o\sigma_m} \int_{-\infty}^{\infty} \mathrm{Exp}\left[-\left(\frac{v_t^2(\sigma_m^2 + \sigma_o^2) - 2v_t(\sigma_m^2 v_o + \sigma_o^2 v_m) + \sigma_m^2 v_o^2 + \sigma_o^2 v_m^2}{2\sigma_o^2\sigma_m^2}\right)\right]\,\mathrm{d}v_t$$

$$\frac{1}{2\pi\sigma_o\sigma_m}\mathrm{Exp}\left[-\left(\frac{\sigma_m^2 v_o^2 + \sigma_o^2 v_m^2}{2\sigma_o^2\sigma_m^2}\right)\right]\int_{-\infty}^{\infty} \mathrm{Exp}\left[-\left(\frac{v_t^2(\sigma_m^2 + \sigma_o^2) - 2v_t(\sigma_m^2 v_o + \sigma_o^2 v_m)}{2\sigma_o^2\sigma_m^2}\right)\right]\,\mathrm{d}v_t$$

now, focusing on the integral,

$$\int_{-\infty}^{\infty} \mathrm{Exp}\left[-\left(\frac{\sigma_m^2 + \sigma_o^2}{2\sigma_o^2\sigma_m^2}\right)\left(v_t^2 - 2v_t\frac{(\sigma_m^2 v_o + \sigma_o^2 v_m)}{\sigma_m^2 + \sigma_o^2}\right)\right]\,\mathrm{d}v_t$$

completing the square gives:

$$\int_{-\infty}^{\infty} \mathrm{Exp}\left[-\left(\frac{\sigma_m^2 + \sigma_o^2}{2\sigma_o^2\sigma_m^2}\right)\left(v_t^2 - 2v_t\frac{(\sigma_m^2 v_o + \sigma_o^2 v_m)}{\sigma_m^2 + \sigma_o^2} + \frac{(\sigma_m^2 v_o + \sigma_o^2 v_m)^2}{(\sigma_m^2 + \sigma_o^2)^2} - \frac{(\sigma_m^2 v_o + \sigma_o^2 v_m)^2}{(\sigma_m^2 + \sigma_o^2)^2}\right)\right]\,\mathrm{d}v_t$$

which simplifies to

$$\int_{-\infty}^{\infty} \mathrm{Exp}\left[-\left(\frac{\sigma_m^2 + \sigma_o^2}{2\sigma_o^2\sigma_m^2}\right)\left(\left(v_t - \frac{(\sigma_m^2 v_o + \sigma_o^2 v_m)}{\sigma_m^2 + \sigma_o^2}\right)^2 - \frac{(\sigma_m^2 v_o + \sigma_o^2 v_m)^2}{(\sigma_m^2 + \sigma_o^2)^2}\right)\right]\,\mathrm{d}v_t$$

where another, non-true term is moved outside of the integral

$$\mathrm{Exp}\left[-\left(\frac{\sigma_m^2+\sigma_o^2}{2\sigma_o^2\sigma_m^2}\right)\left(-\frac{(\sigma_m^2 v_o+\sigma_o^2 v_m)^2}{(\sigma_m^2+\sigma_o^2)^2}\right)\right]\int_{-\infty}^{\infty}\mathrm{Exp}\left[-\left(\frac{\sigma_m^2+\sigma_o^2}{2\sigma_o^2\sigma_m^2}\right)\left(\left(v_t-\frac{(\sigma_m^2 v_o+\sigma_o^2 v_m)}{\sigma_m^2+\sigma_o^2}\right)^2\right)\right]\,\mathrm{d}v_t$$

now, for simplicity, set:

$$\frac{(\sigma_m^2 v_o+\sigma_o^2 v_m)}{\sigma_m^2+\sigma_o^2}=\alpha\,;\qquad \frac{\sigma_m^2+\sigma_o^2}{2\sigma_o^2\sigma_m^2}=\frac{1}{\beta^2}\,;\qquad \frac{\sigma_m^2 v_o^2+\sigma_o^2 v_m^2}{2\sigma_o^2\sigma_m^2}=\zeta$$

then, the forgoing equation becomes

$$\mathrm{Exp}\left[\frac{\alpha^2}{\beta^2}\right]\int_{-\infty}^{\infty}\mathrm{Exp}\left[-\frac{(v_t-\alpha)^2}{2\beta^2}\right]\,\mathrm{d}v_t$$

and if put back into the full equation before we focused on the integral:

$$\frac{1}{2\pi\sigma_o\sigma_m}\mathrm{Exp}\left[-\zeta\right]\mathrm{Exp}\left[\frac{\alpha^2}{\beta^2}\right]\int_{-\infty}^{\infty}\mathrm{Exp}\left[-\frac{(v_t-\alpha)^2}{2\beta^2}\right]\,\mathrm{d}v_t$$

$$\frac{1}{2\pi\sigma_o\sigma_m}\mathrm{Exp}\left[\frac{\alpha^2}{\beta^2}-\zeta\right]\int_{-\infty}^{\infty}\mathrm{Exp}\left[-\frac{(v_t-\alpha)^2}{2\beta^2}\right]\,\mathrm{d}v_t$$

$$\frac{1}{2\pi\sigma_o\sigma_m}\mathrm{Exp}\left[\frac{\alpha^2}{\beta^2}-\zeta\right]\frac{\beta\sqrt{2\pi}}{\beta\sqrt{2\pi}}\int_{-\infty}^{\infty}\mathrm{Exp}\left[-\frac{(v_t-\alpha)^2}{2\beta^2}\right]\,\mathrm{d}v_t$$

as

$$\frac{1}{\beta\sqrt{2\pi}}\int_{-\infty}^{\infty}\mathrm{Exp}\left[-\frac{(v_t-\alpha)^2}{2\beta^2}\right]\,\mathrm{d}v_t=1$$

$$P(d|m)=\frac{1}{2\pi\sigma_o\sigma_m}\mathrm{Exp}\left[\frac{\alpha^2}{\beta^2}-\zeta\right]\beta\sqrt{2\pi}$$

$$\boxed{P(d|m)=\frac{\beta}{\sigma_o\sigma_m\sqrt{2\pi}}\mathrm{Exp}\left[\frac{\alpha^2}{\beta^2}-\zeta\right]}$$

which is completely free of a true parameter.

Appendix B

Coordinate transformations

The natural way of calculating circular velocity is in a Galactocentric Cylindrical (GCY) frame of reference. As the observational data is given in Equatorial Coordinates (EC, a natural frame of reference for an observer), there ought to be a set of coordinate transformations which take me from one frame to the other. For simplicity's sake, the first task becomes converting the GCY frame to the Heliocentric Galactic Polar (HGP) frame.

The position of an object on the sky can be determined from knowing three parameters in the HGP frame. These are, the longitude ℓ, the latitude b and the parallax ϖ. This frame of reference, in the Galactic plane ($z = 0 \Rightarrow b = 0$), is shown in Figure B.1. It is easier to express HGP coordinates in terms of its corresponding Cartesian coordinates (HCA) as follows:

$$x = r * \cos(\ell), \qquad y = r * \sin(\ell), \qquad v_r = \mathrm{d}r/\mathrm{d}t, \qquad \mu_\ell = \mathrm{d}\ell/\mathrm{d}t, \qquad r = 1/\varpi. \quad \text{(B.1)}$$

The expressions for the x and y coordinates in the HCA frame (Eq. (B.1)) is converted into the Galactocentric frame, which is shown as the blue in Figure B.1. The x and y coordinates in the Galactocentric Cartesian frame of reference (GCA) as a function of HCA coordinates can be derived by the following transformation:

$$x_{\mathrm{GCA}} = R_0 - x_{\mathrm{HCA}}, \qquad y_{\mathrm{GCA}} = -y_{\mathrm{HCA}}. \quad \text{(B.2)}$$

Finally, an expression for the radius R and the angle ϕ in terms of the Galactocentric Cylindrical coordinates (GCY) can be obtained:

$$R = \sqrt{y_{\mathrm{GCA}}^2 + y_{\mathrm{GCA}}^2}, \qquad \phi = \tan^{-1}(y_{\mathrm{GCA}}/x_{\mathrm{GCA}}) \quad \text{(B.3)}$$

where, R is pointing from the Galactic center towards an object in the plane and pivotally, the angular velocity of ϕ is equivalent to the circular velocity

$$v_\phi = V_c(R).$$

Once the circular velocity has been obtained in the GCY frame, it is possible to decompose it into the two observable velocity components in the HGP frame which can then finally be transformed into the EC frame. First, the velocity components are expressed in the HCA frame as follows:

$$v_{x,\mathrm{HCA}} = v_\phi \sin(\phi), \qquad v_{y,\mathrm{HCA}} = -v_\phi \cos(\phi) - V_\odot, \quad \text{(B.4)}$$
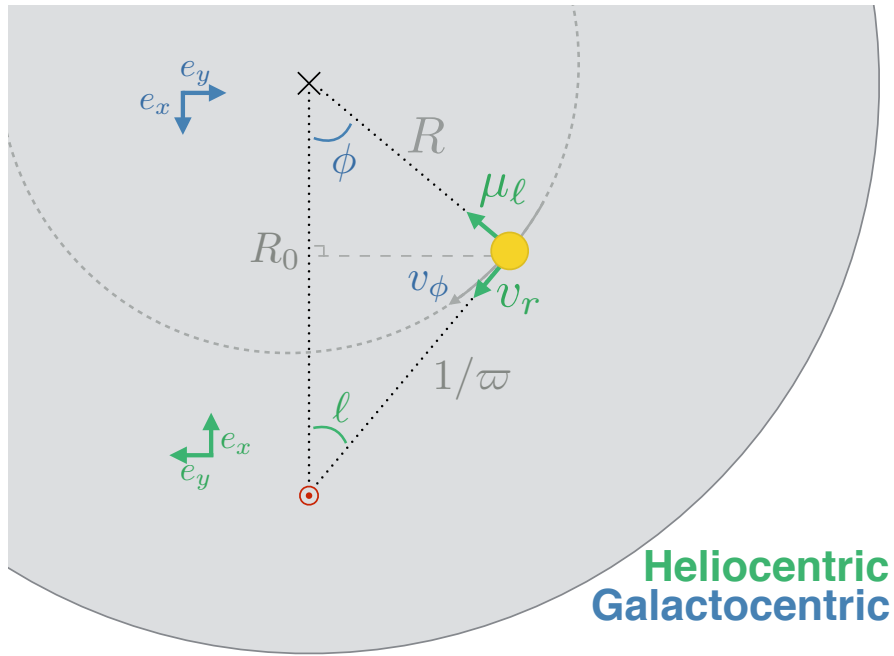
Figure B.1: Plan view of the Galaxy in Heliocentric Galactic Polar coordinates (HGP, green) and Galactocentric Cylindrical coordinates (GCY, blue). Here, $v_\phi = V_c$. The red circle represents the Sun, the black cross represents the Galactic center and the yellow circle represents a point source of light. Green shows the observable velocity components: the longitudinal proper motion, μ_ℓ, and the radial velocity, v_r.

Finding the expression for v_r and v_t.
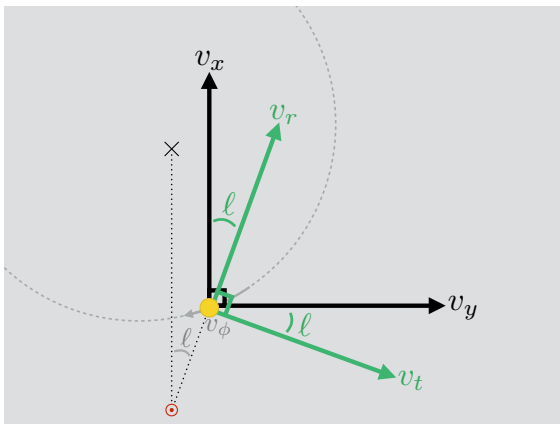
Figure B.2: The Heliocentric frame of reference. In black: the HCA frame and in green: the HGP frame.
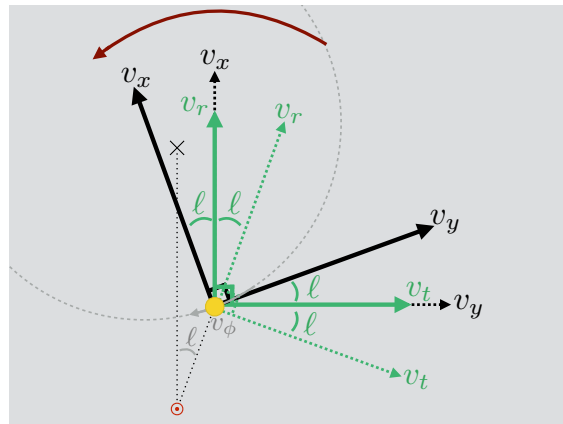
Figure B.3: Both frames are rotated such that the HGP frame is in line with the imaginary line between the Sun and the Galactic center.
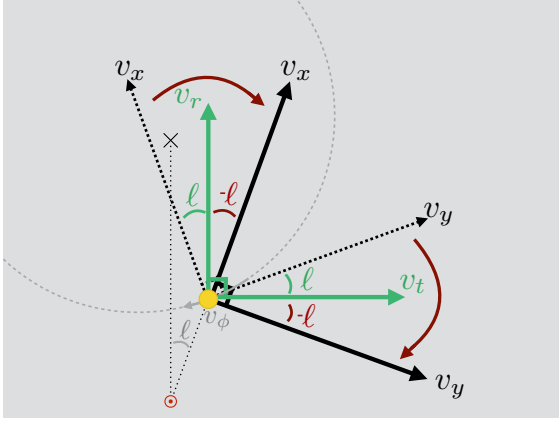
Figure B.4: The HCA frame is rotated such that..?
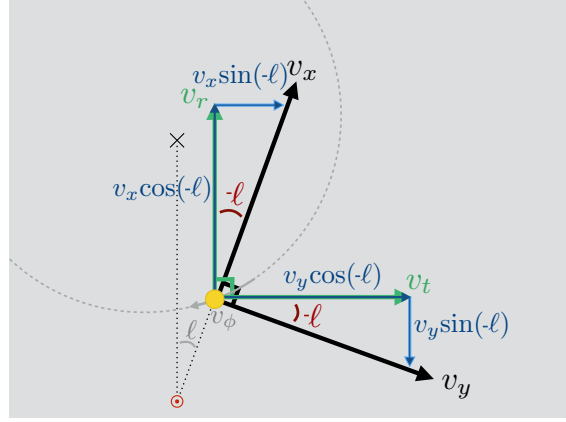
Figure B.5: In blue: the velocity components that will make up the observables.

where $V_\odot$ is the velocity of the Sun in y direction. Now, once in the Heliocentric frame, some clever coordinate transformations are applied, which are illustrated in Figures B.2 - B.5.

The HGP velocity components (tangential and radial velocity, v_t and v_r) can now be expressed in terms of the aforementioned HCA coordinates indicated in blue in Figure B.5

$$v_t = v_x \sin(-\ell) + v_y \cos(-\ell), \qquad v_r = v_x \cos(-\ell) - v_y \sin(-\ell). \tag{B.5}$$

One can then of course turn the tangential velocity in Eq. (B.5) into a proper motion by

$$\mu_\ell = v_t \varpi.$$

The very last step is to remain in the Heliocentric frame and convert the HGP coordinates to the Heliocentric Equatorial Polar (HEQ) or commonly called the Equatorial coordinate system (EC). This last step is more complicated and the reader should trust that there is code that transforms HGP coordinates into the ECs

$$\mu_a(\mu_\ell); \qquad \mu_d(\mu_\ell).$$

We have now gone full circle and the steps can be summarized as follows

Model in GCY, observations in EC, Do: EC(HGP(HCA(GCY)))

Table 4.2 shows the comparable components.

Appendix C

Constraints

C.1 Disk constraint

The disk parameters a_2 and b_2 are constrained by relating these to the observationally determined values for an exponential disk model. The mass ratio within and outside of a set radius for both a Miyamoto-Nagai (MN) disk and an exponential (exp) disk is set equal. In effect, an expression for a_2 and b_2 as a function of observationally found parameters is recovered.

The MN and exponential disk profiles

$$\rho_{\mathrm{MN}} = \left(\frac{b^2 M}{4\pi}\right) \frac{aR^2 \left(a + 3\sqrt{b^2 + z^2}\right) \left(a + \sqrt{b^2 + z^2}\right)^2}{\left[\left(a + \sqrt{b^2 + z^2}\right)^2 + R^2\right]^{5/2} (b^2 + z^2)^{3/2}}; \qquad \rho_{\exp} = \frac{\Sigma_0}{2z_d} e^{-R/R_d} e^{-|z|/z_d},$$

(C.1)

are first transformed into their corresponding surface density profiles in order to find their mass distribution. The surface density is retrieved by integrating over the entire vertical space in the plane,

$$\Sigma(R) = \int_{-\infty}^{\infty} \rho(R, z) \, \mathrm{d}z.$$

For the exponential disk, the surface density becomes

$$\Sigma_{\exp}(R) = \frac{\Sigma_0}{2z_d} e^{-R/R_d} \int_{-\infty}^{\infty} e^{-|z|/z_d} \, \mathrm{d}z = \Sigma_0 \, e^{-R/R_d}$$

Conversely, the MN density profile does not have a straight-forward simple analytical solution. For this reason, an approximation is made and a close alternative to the MN disk is invoked, namely the Kuzmin (K) surface density profile

$$\Sigma_{\mathrm{K}}(R) = \frac{aM}{2\pi \left(R^2 + a^2\right)^{3/2}}.$$

Since a mass element $\mathrm{d}M$ inside of a circular surface is

$$M(R) = \int_{R_1}^{R_2} 2\pi R \, \Sigma(R) \, \mathrm{d}R,$$

the mass ratios within and outside of R_0 for an exponential and a Kuzmin disk become

$$\frac{M_{\mathrm{K}}(R=0<R_0)}{M_{\mathrm{K}}(R>R_0)} = \frac{\int_0^{R_0} R(R^2+a^2)^{-3/2}\,\mathrm{d}R}{\int_{R_0}^{\infty} R(R^2+a^2)^{-3/2}\,\mathrm{d}R}; \qquad \frac{M_{\mathrm{exp}}(R=0<R_0)}{M_{\mathrm{exp}}(R>R_0)} = \frac{\int_0^{R_0} R\,e^{-R/R_d}\,\mathrm{d}R}{\int_{R_0}^{\infty} R\,e^{-R/R_d}\,\mathrm{d}R}.$$

These mass ratios simplify to

$$M_{\mathrm{ratio,K}} = \frac{\sqrt{R_0^2+a^2}}{a} - 1; \qquad M_{\mathrm{ratio,exp}} = \frac{R_d\,e^{R_0/R_d}}{R_0+R_d} - 1. \tag{C.2}$$

The mass ratios in Eq. (C.2) are equated and solved for a_2 which yields

$$a_2(R_d) = \frac{R_0(R_0+R_d)}{\sqrt{R_d^2\,e^{2R_0/R_d} - (R_0+R_d)^2}}. \tag{C.3}$$

The solution of the Kuzmin scale length a_2 (which will be used as an MN scale length) as a function of an exponential disk scale height R_d can be seen in Figure C.1.
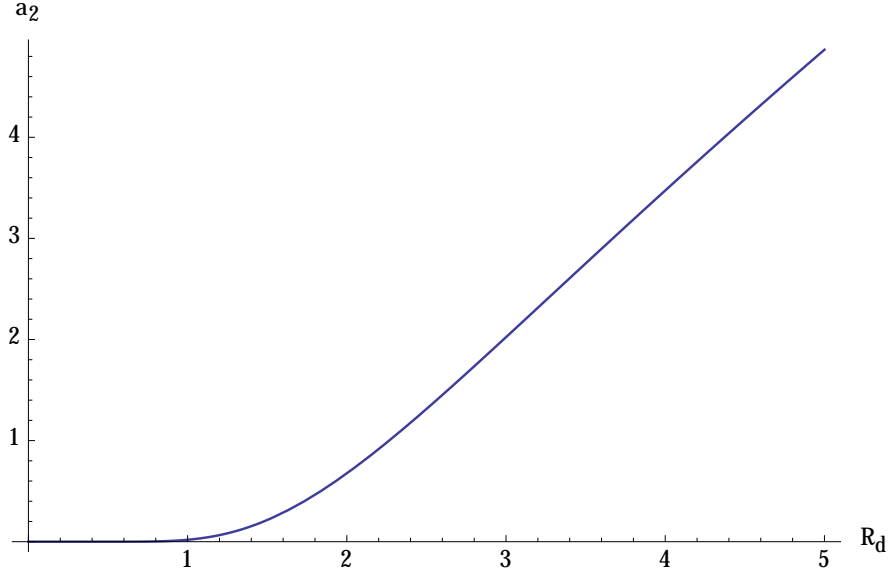
Figure C.1: Analytical solution to a Kuzmin disk scale length a_2 as a function of an exponential disk scale length R_d, calculated by equating the mass ratio $M(R<R_0)/M(R>R_0)$ for the two models.

Bland-Hawthorn & Gerhard (2016) found the exponential disk scale length to be $R_d = 2.5 \pm 0.4$ kpc as an average of many studies. That corresponds to the normal distribution $P(R_d) = G(R_d|2.5, 0.4)$. To find the desired pdf of a_2, the following condition is set up

$$P(a_2) = P(R_d)\frac{\mathrm{d}R_d}{\mathrm{d}a_2}. \tag{C.4}$$

The derivative term becomes

$$\left(\frac{\mathrm{d}a_2}{\mathrm{d}R_d}\right)^{-1} = e^{-2R_0/R_d}\left(e^{2R_0/R_d} - (R_0+R_d)^2\right)^{3/2} R_0^{-3}. \tag{C.5}$$

Inserting Eq. (C.5) into Eq (C.4) gives

$$P(a_2) = G(R_d|2.5, 0.4) \times e^{-2R_0/R_d} \left(e^{2R_0/R_d} - (R_0 + R_d)^2 \right)^{3/2} R_0^{-3} \qquad (C.6)$$

which can be seen in Figure C.2
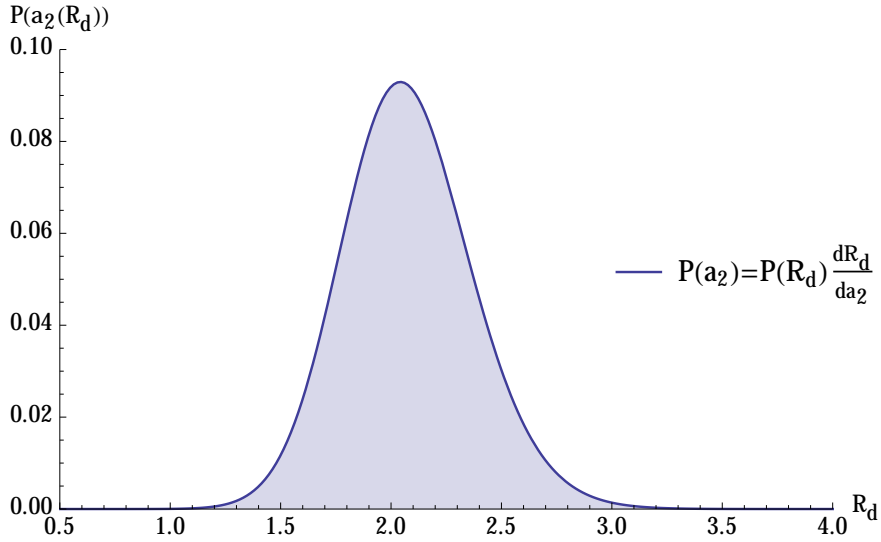
Figure C.2: Probability of a Kuzmin disk scale length a_2 given an exponential disk scale length R_d.

From Figure C.2 we see that the pdf behaves normally and can therefore be used as a constraint and thus as a prior in the model. Finally, from here, the scale length MN b_2 can simply be found by the relation $b_2 = 0.2\, a_2$ (Binney & Tremaine 2011).

C.2 Bulge constraint

Slightly changing the methodology from that described in section C.1, we wish to construct a relation between a MN scale length and height a_1 and b_2 as functions of parameters, this time obtained from a model by Bissantz & Gerhard (2002), henceforth referred to as BG. This model aims to describe the mass density profile of the bulge. As this model is not axisymmetric, an axisymmetric approximation is made (McMillan 2011)

$$\rho_{BG} = \frac{\rho_{b,0}}{(1 + r'/r_0)^{1.8}} e^{-(r'/r_{cut})^2}, \qquad (C.7)$$

where, in cylindrical coordinates, $r' = \sqrt{R^2 + (z/q)^2}$ and where $r_0 = 0.075$ kpc, $r_{cut} = 2.1$ kpc, $q = 0.5$.

A parameter that has to be taken into account is q, which scales the z axis ($q < 1$ gives an oblate spheroid). A shell of mass dm in this geometry becomes $dm = 4\pi q r'^2 \rho(r') dr'$. The bulge will be defined outward to a bulge cut off region $R_{bc} = 3.5$ kpc. The total mass becomes

$$M(r' < R_{bc}) = 4\pi q \int_0^{R_{bc}} r'^2 \rho_{BG}(r')\, dr' = 4\pi q \rho_{b,0} \int_0^{R_{bc}} \frac{r'^2 e^{-(r'/r_{cut})^2}}{(1 + r'/r_0)^{1.8}}\, dr'. \qquad (C.8)$$

where the chosen model for the bulge density, Eq. (C.7), is inserted. Numerically, the mass ratio within and outside of a bulge cut off radius $R_{bc} = 3.5$ kpc becomes

$$\frac{M_{BG}(R = 0 < R_{bc})}{M_{BG}(R > R_{bc})} = \frac{0.0139462}{0.000412596} \tag{C.9}$$

and for the Kuzmin surface density

$$\frac{M_K(R = 0 < R_{bc})}{M_K(R > R_{bc})} = \frac{\int_0^{R_{bc}} R(R^2 + a^2)^{-3/2}\,\mathrm{d}R}{\int_{R_{bc}}^{\infty} R(R^2 + a^2)^{-3/2}\,\mathrm{d}R}. \tag{C.10}$$

These mass ratios simplify to

$$M_{\mathrm{ratio,BG}} = 33.8; \qquad M_{\mathrm{ratio,K}} = \frac{\sqrt{R_{bc}^2 + a_1^2}}{a_1} - 1 \tag{C.11}$$

The mass ratios Eq. (C.11) are equated and solved for a_1 which yields

$$a_1(R_{bc}) = 0.0295978\,R_{bc}. \tag{C.12}$$

If $R_{bc} = 3.5$ kpc, $a_1 = 0.103592$ kpc and as $b_1 = 0.5a_1$ (Bissantz & Gerhard 2002; Reid et al. 2014), $b_1 = 0.0517962$ kpc.

Appendix D

Adding exponential decay to the spiral perturbation terms

To further test models of spiral structure I add an extra term to the spiral perturbation motivated by the fact that the stars and gas are well described by exponential models, namely

$$\mathrm{Exp}\left[\frac{R_0 - R}{R_d}\right], \tag{D.1}$$

where R_d is the exponential disk scale length. As such, adding this term to the BB model for spiral perturbation results in the following expressions

$$V_R = f_R \cos\chi \times \mathrm{Exp}\left[(R_0 - R)/R_d\right]; \qquad \Delta V_\phi = f_\theta \sin\chi \times \mathrm{Exp}\left[(R_0 - R)/R_d\right].$$

D.1   Results

(a) Azimuthal velocity map.

(b) Radial velocity map.
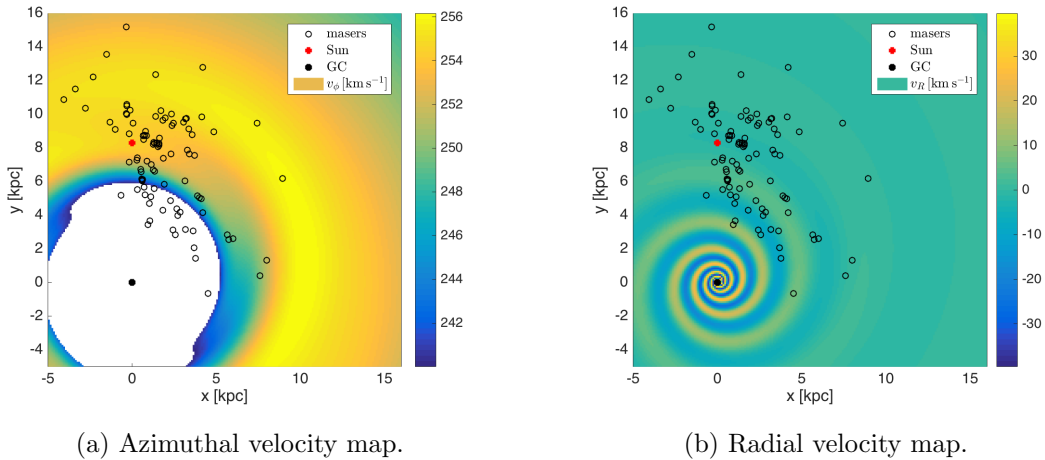
Figure D.1: Velocity maps for the best-fitting parameters in the interval $-5 \leq x, y \leq 16$. Here, the spiral model has 2 arms and the bulge cut off radius $R_{\mathrm{bc}} = 3.5$ kpc.
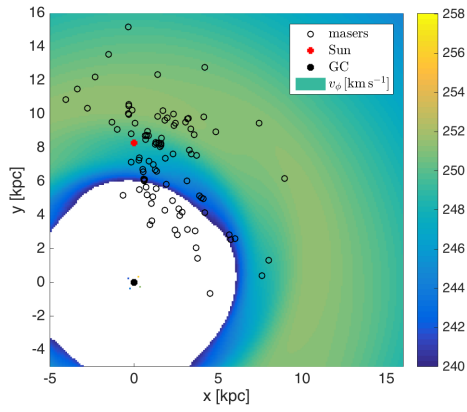
(a) Azimuthal velocity map.
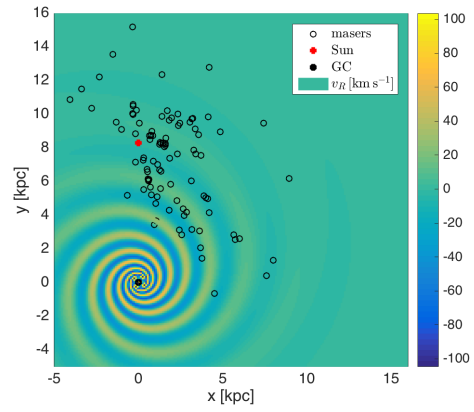
(b) Radial velocity map.

Figure D.2: Velocity maps for the best-fitting parameters in the interval $-5 \leq x, y \leq 16$. Here, the spiral model has 4 arms and the bulge cut off radius $R_{\mathrm{bc}} = 3.5$ kpc.
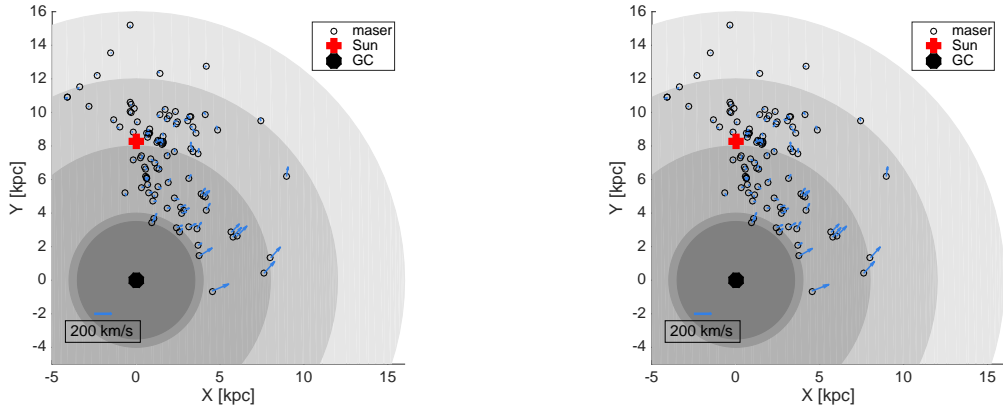
(a) Maser data versus axisymmetric model.

(b) Maser data versus spiral perturbation model.
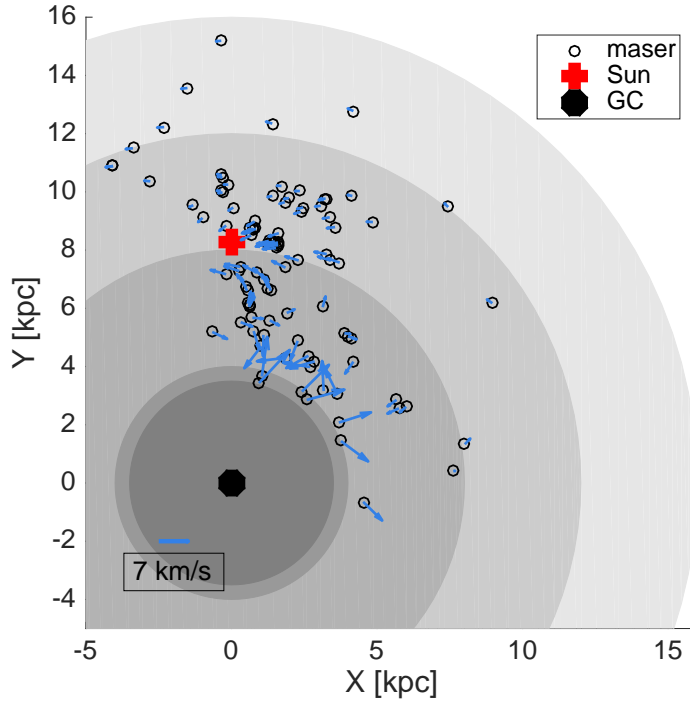
(c) Axisymmetric model versus spiral perturbation model.

Figure D.3: The residuals between the observed and modeled velocity components of masers. Data given by Reid et al. (2014). The gray scale is indicates 5 kpc radial increments except for the first one close to the Galactic center with indicates the bulge cut off radius. Here, the spiral model has 2 arms and the bulge cut off radius $R_{\rm bc} = 3.5$ kpc.
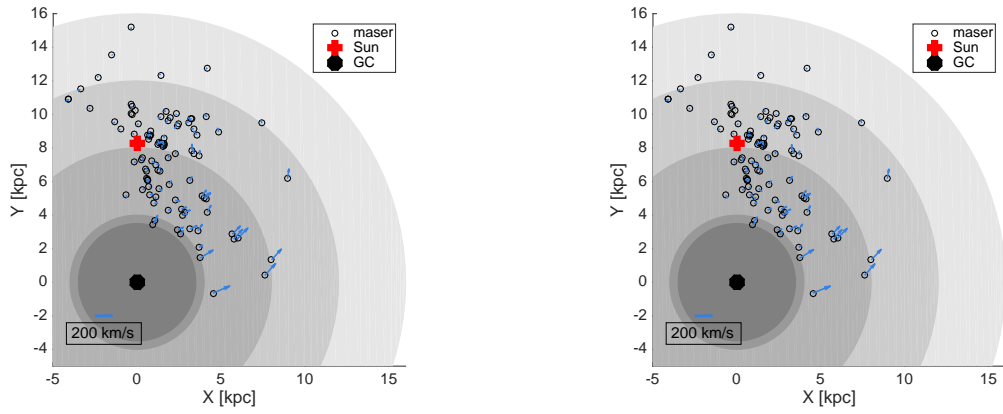
(a) Maser data versus axisymmetric model.

(b) Maser data versus spiral perturbation model.
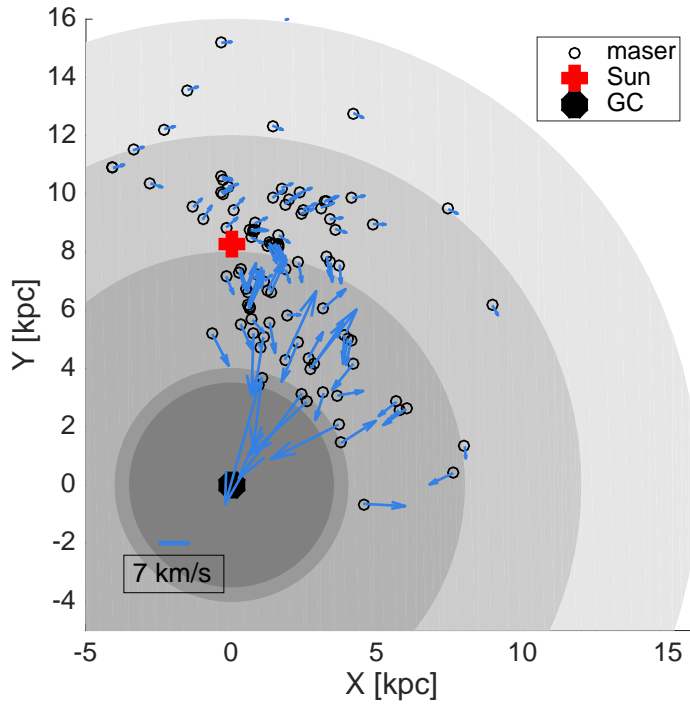
(c) Axisymmetric model versus spiral perturbation model.

Figure D.4: The residuals between the observed and modeled velocity components of masers. Data given by Reid et al. (2014). Here, the spiral model has 4 arms and the bulge cut off radius $R_{\mathrm{bc}} = 3.5$ kpc.
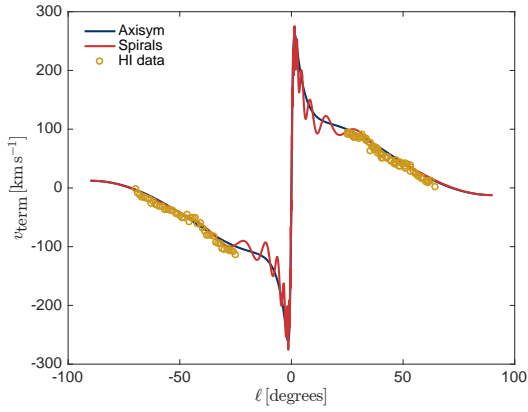
(a) Azimuthal velocity map.
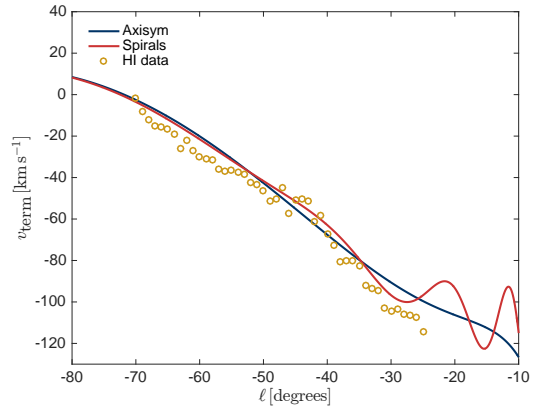
(b) Radial velocity map.

Figure D.5: (a) shows the terminal velocity (line of sight velocity) of HI line emission as a function of Galactic longitude, ℓ. The lines represents the best-fit models, (blue: axisymmetric; red: spiral perturbation) and circles show the observed values Malhotra (1995). (b) shows a zoomed in version of (a) to better show the difference between the models. Here, the spiral model has 2 arms and the bulge cut off radius $R_{\mathrm{bc}} = 3.5$ kpc.
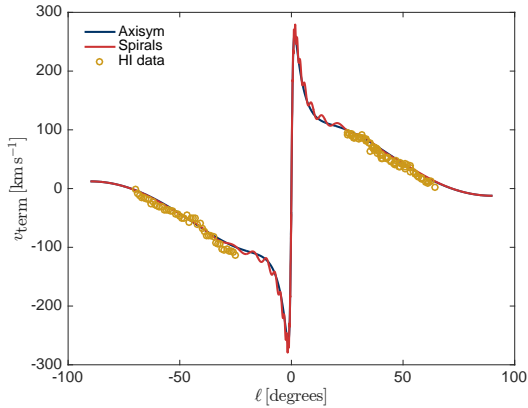

(a) Azimuthal velocity map.
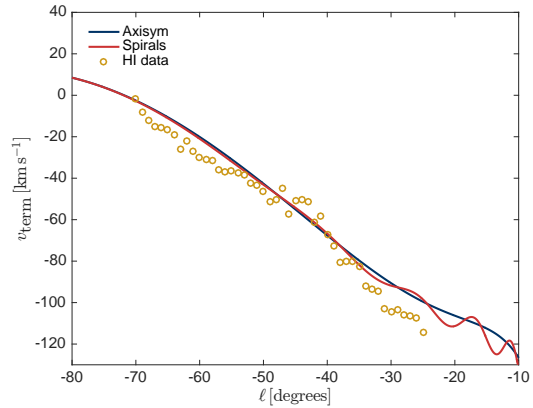
(b) Radial velocity map.

Figure D.6: (a) shows the terminal velocity (line of sight velocity) of HI line emission as a function of Galactic longitude, ℓ. The lines represents the best-fit models, (blue: axisymmetric; red: spiral perturbation) and circles show the observed values Malhotra (1995). (b) shows a zoomed in version of (a) to better show the difference between the models. Here, the spiral model has 4 arms and the bulge cut off radius $R_{\mathrm{bc}} = 3.5$ kpc.

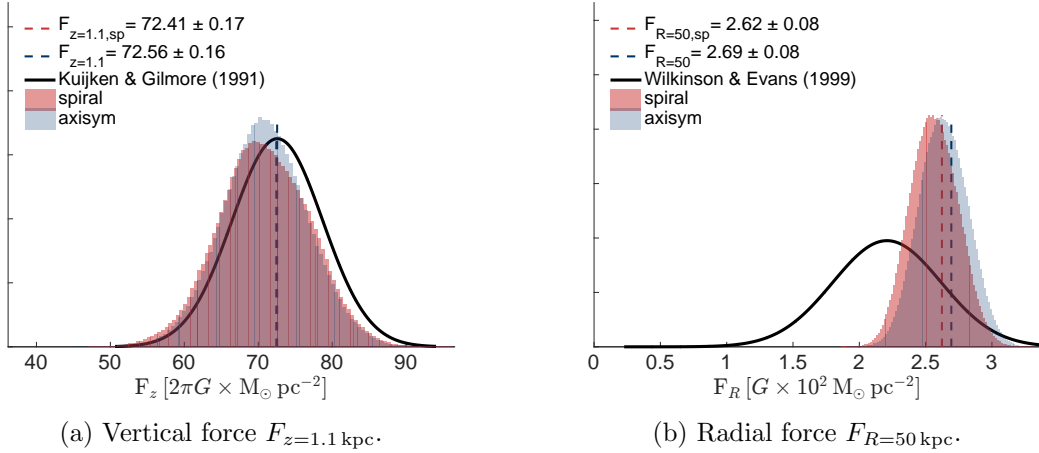(a) Vertical force $F_{z=1.1\,\mathrm{kpc}}$.

(b) Radial force $F_{R=50\,\mathrm{kpc}}$.
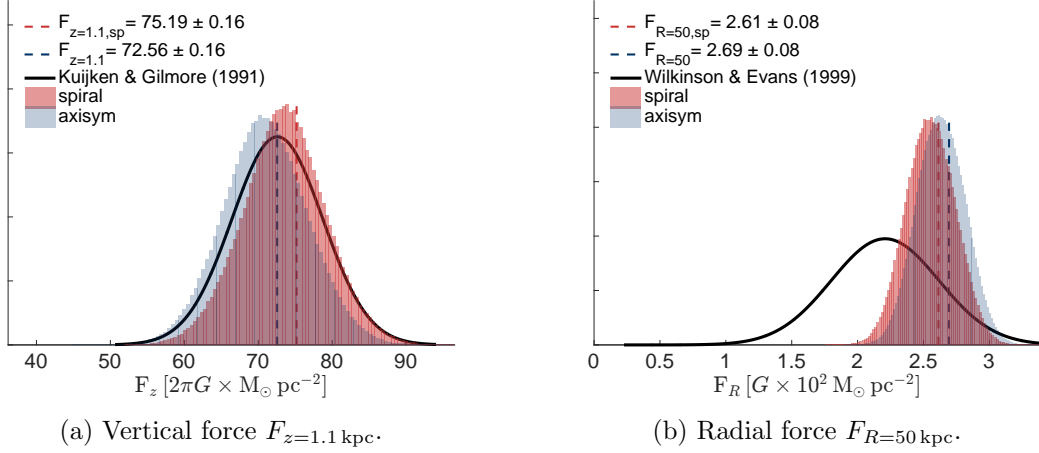
Figure D.7: Histogram showing (left) the vertical force per unit mass an object in the Galaxy would be subject to at $R = R_0$ and $z = 1.1$ kpc above the plane and (right) the radial force an object in the Galaxy would be subject to at $R = 50$ kpc and $z = 0$. Solid line shows estimates by Kuijken & Gilmore (1991) and Wilkinson & Evans (1999) respectively. The dashed line indicates the expectation value. Red histograms represents the spiral arm model and blue the axisymmetric model. Here, the spiral model has 2 arms and the bulge cut off radius $R_{\mathrm{bc}} = 3.5$ kpc.

(a) Vertical force $F_{z=1.1\,\mathrm{kpc}}$.

(b) Radial force $F_{R=50\,\mathrm{kpc}}$.

Figure D.8: Histogram showing (left) the vertical point mass force per unit mass an object in the Galaxy would be subject to at $R = R_0$ and $z = 1.1$ kpc above the plane and (right) the radial force an object in the Galaxy would be subject to at $R = 50$ kpc and $z = 0$. Solid line shows estimates by Kuijken & Gilmore (1991) and Wilkinson & Evans (1999) respectively. The dashed line indicates the expectation value. Red histograms represents the spiral arm model and blue the axisymmetric model. Here, the spiral model has 4 arms and the bulge cut off radius $R_{\mathrm{bc}} = 3.5$ kpc.

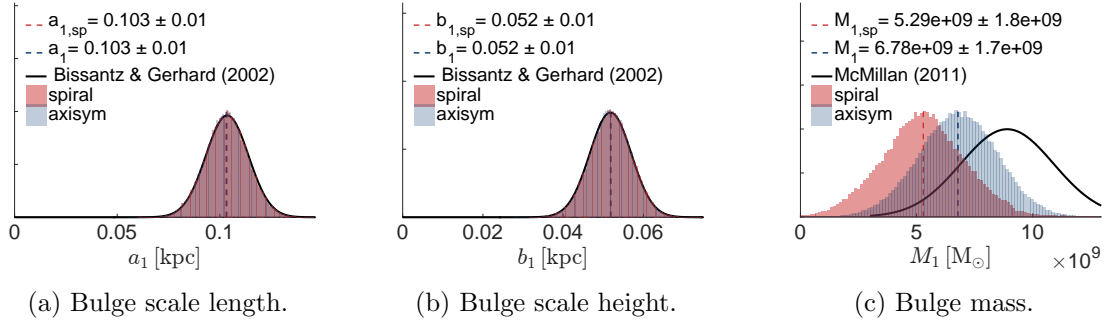(a) Bulge scale length.

(b) Bulge scale height.

(c) Bulge mass.

Figure D.9: Histograms of the axisymmetric spheroidal bulge with MN scale length a_1, scale height b_1 and mass M_1 with and without spiral perturbations (red and blue respectively). The dashed line indicates the expectation value. Here, the spiral model has 2 arms and the bulge cut off radius $R_{\rm bc} = 3.5$ kpc. The solid lines represent the priors listed in table 4.1.
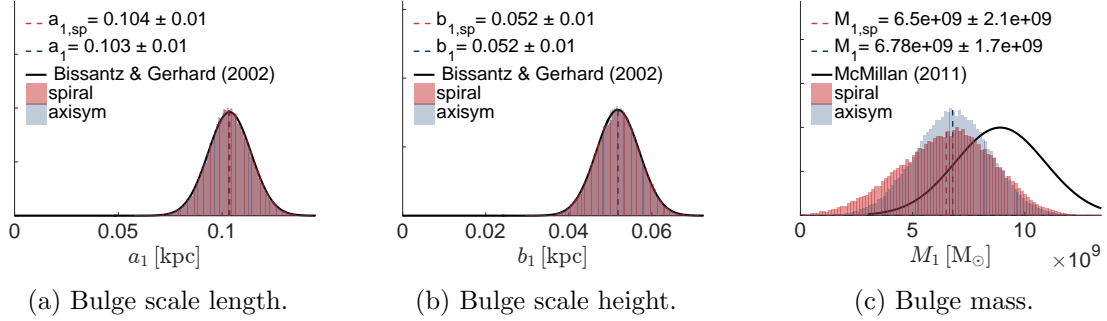

(a) Bulge scale length.

(b) Bulge scale height.

(c) Bulge mass.

Figure D.10: Histograms of the axisymmetric spheroidal bulge with MN scale length a_1, scale height b_1 and mass M_1 with and without spiral perturbations (red and blue respectively). The dashed line indicates the expectation value. Here, the spiral model has 4 arms and the bulge cut off radius $R_{\rm bc} = 3.5$ kpc. The solid lines represent the priors listed in table 4.1.
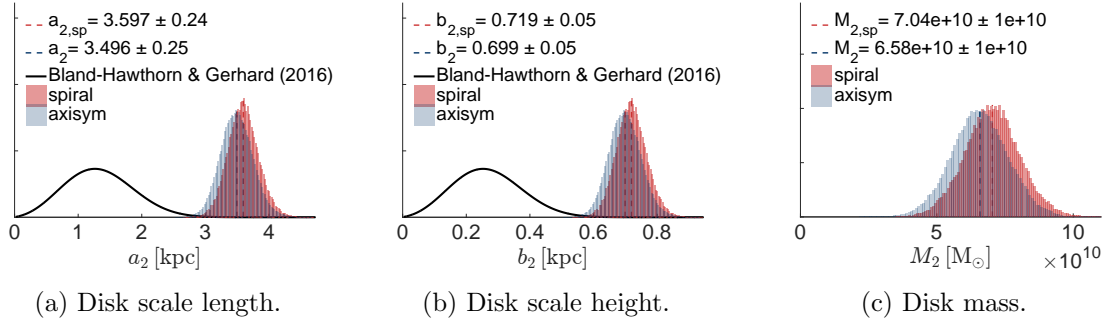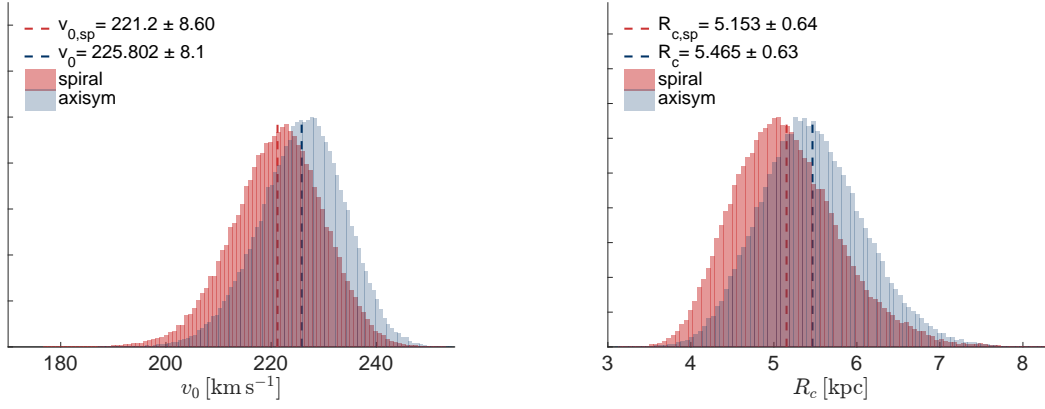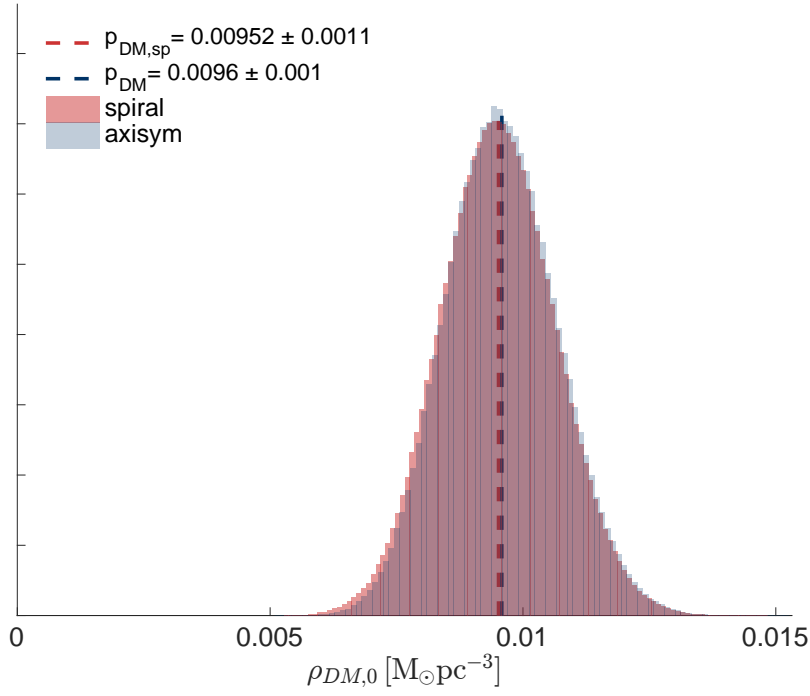
Figure D.11: Histograms of the axisymmetric spheroidal disk with MN scale length a_2, scale height b_2 and mass M_2 with and without spiral perturbations (red and blue respectively). The dashed line indicates the expectation value. Here, the spiral model has 2 arms and the bulge cut off radius $R_{\mathrm{bc}} = 3.5$ kpc. The solid lines represent the priors listed in table 4.1.
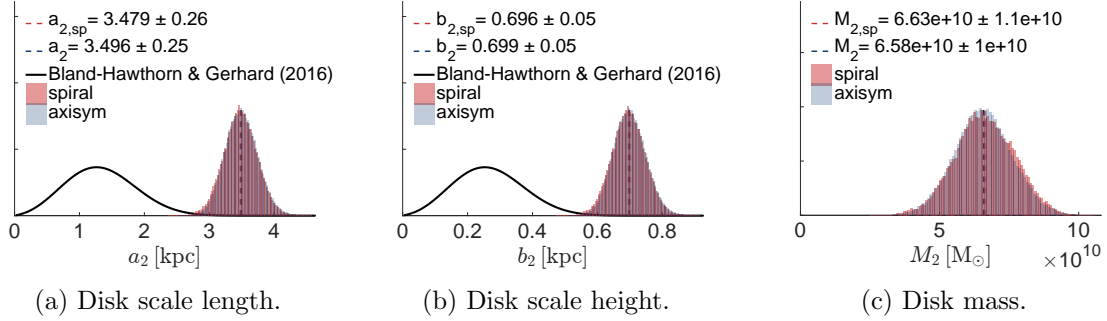
Figure D.12: Histograms of the axisymmetric spheroidal disk with MN scale length a_2, scale height b_2 and mass M_2 with and without spiral perturbations (red and blue respectively). The dashed line indicates the expectation value. Here, the spiral model has 4 arms and the bulge cut off radius $R_{\mathrm{bc}} = 3.5$ kpc. The solid lines represent the priors listed in table 4.1.
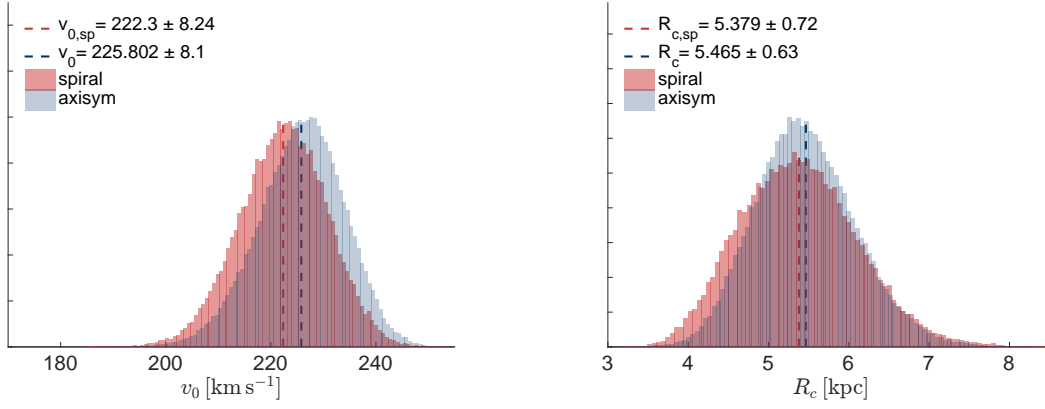
(a) Halo maximum velocity v_0.
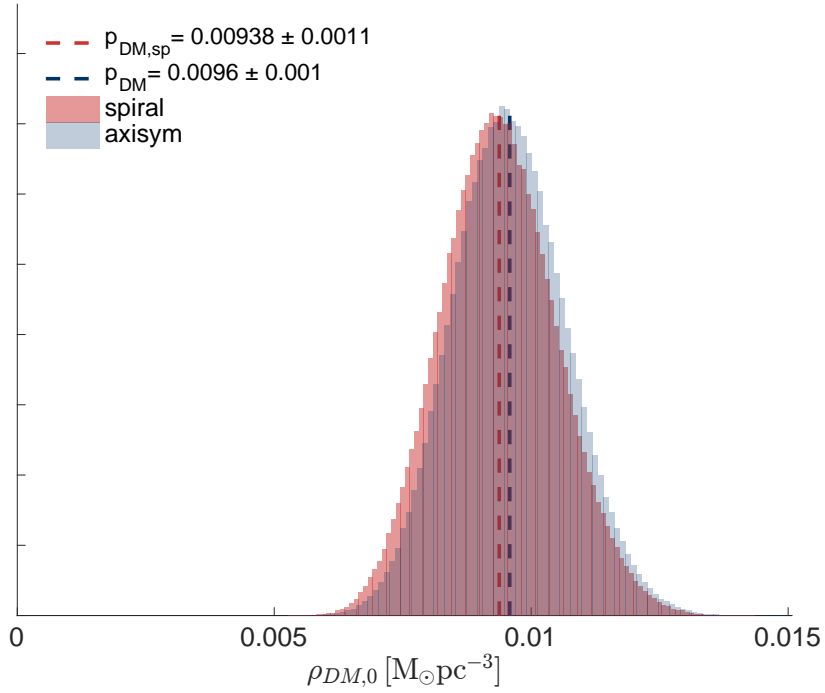
(b) Halo core radius R_c.

(c) Local DM density.

Figure D.13: Histogram of the logarithmic halo parameters v_0 (a), R_c (b) and (c) shows the local DM density. Red histograms represents the spiral arm model and blue the axisymmetric model. Here, the spiral model has 2 arms and the bulge cut off radius $R_{\mathrm{bc}} = 3.5$ kpc.
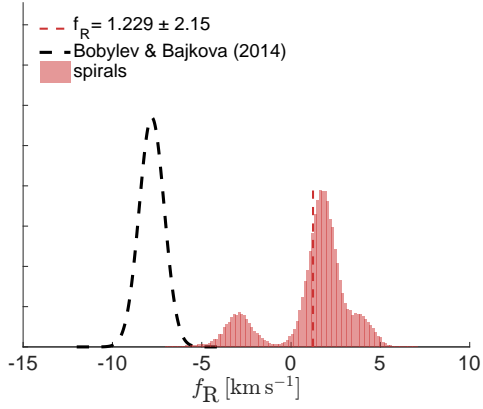
(a) Halo maximum velocity v_0.
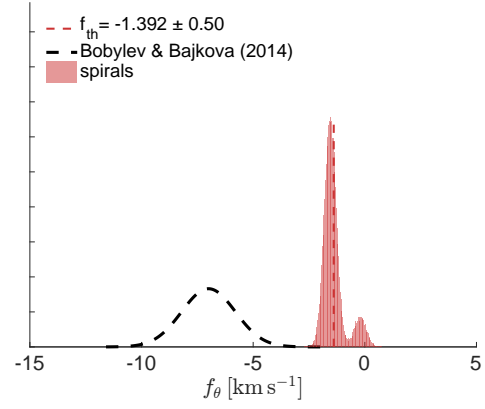
(b) Halo core radius R_c.
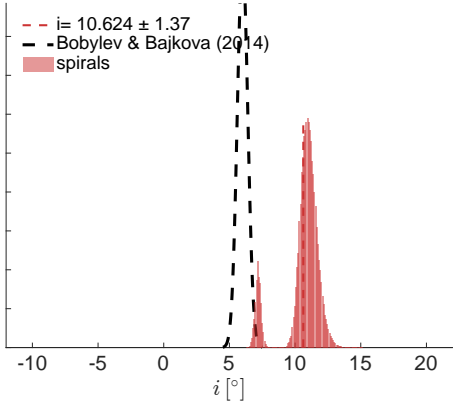

(c) Local DM density.

Figure D.14: Histogram of the logarithmic halo parameters v_0 (a), R_c (b) and (c) shows the local DM density. Red histograms represents the spiral arm model and blue the axisymmetric model. Here, the spiral model has 4 arms and the bulge cut off radius $R_{\mathrm{bc}} = 3.5$ kpc.

(a) Spiral radial velocity amplitude.

(b) Spiral azimuthal velocity amplitude.

(c) Spiral pattern pitch angle.
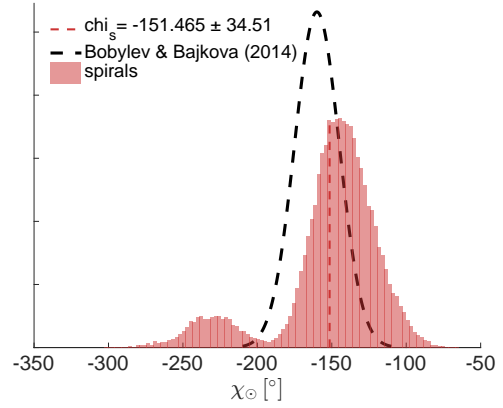
(d) Radial phase of the Sun $\chi_\odot$.

Figure D.15: Histograms of the spiral perturbation parameters. (a) and (b) show the wave amplitude strengths for f_R and f_θ respectively. (c) and (d) show the wave pitch angle i and radial phase of the Sun $\chi_\odot$ respectively. Dashed lines represent results from Bobylev & Bajkova (2014) which used a 2 armed model. Here, the spiral model has 2 arms and the bulge cut off radius $R_{\mathrm{bc}} = 3.5$ kpc.

(a) Spiral radial velocity amplitude.

(b) Spiral azimuthal velocity amplitude.

(c) Spiral pattern pitch angle.
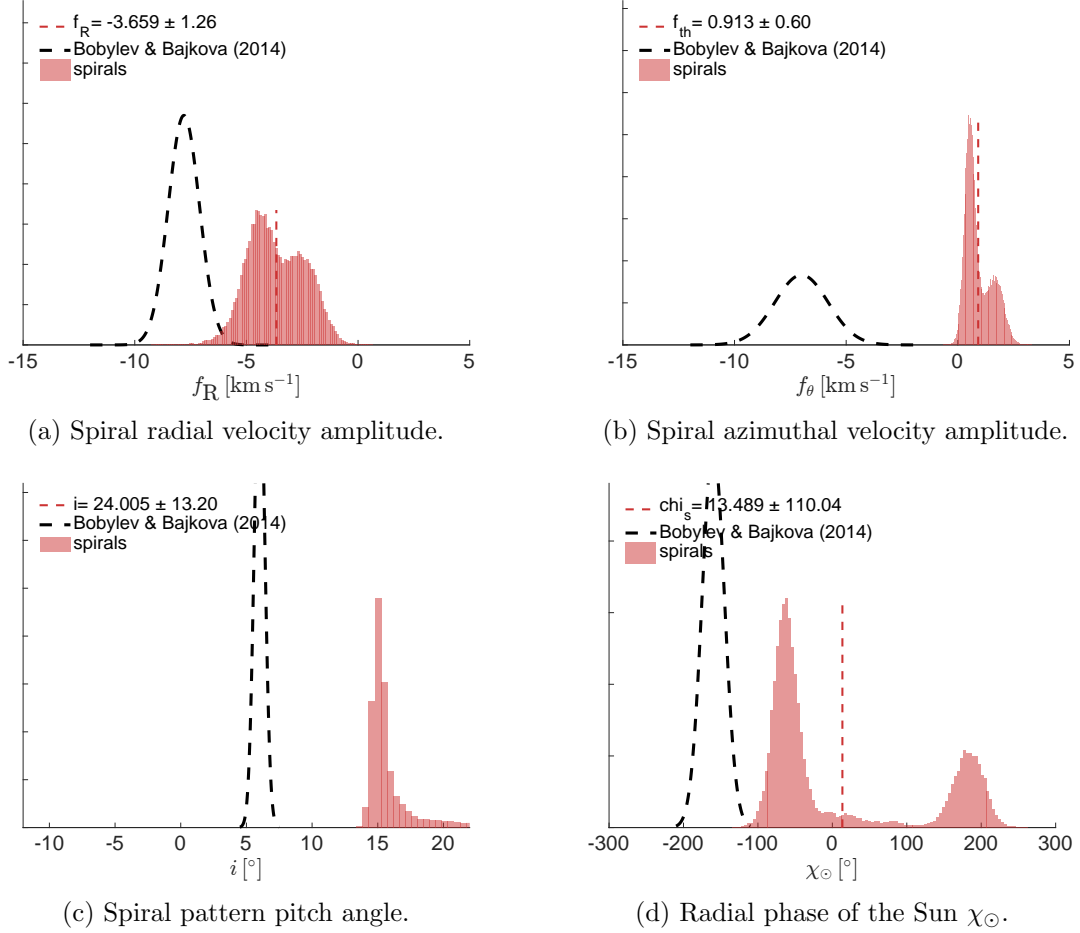
(d) Radial phase of the Sun $\chi_\odot$.

Figure D.16: Histograms of the spiral perturbation parameters. (a) and (b) show the wave amplitude strengths for f_R and f_θ respectively. (c) and (d) show the wave pitch angle i and radial phase of the Sun $\chi_\odot$ respectively. Dashed lines represent results by Bobylev & Bajkova (2014) which used a 4 armed model. Here, the spiral model has 4 arms and the bulge cut off radius $R_{\mathrm{bc}} = 3.5$ kpc.

D.2   Conclusion

From the above Figure it is reassuring to see that the pdfs did not change significantly compared to that without the added exponential term. However, when looking at the spiral arm terms in Figures D.15 and D.16, there are some wandering going on in the MCMC chain. It seems as though with this new model, there are some other values for the spiral parameters that are preferred.

The big difference is when looking at the velocity maps in Figures D.1 and D.2.

The main result here is the large radial velocity perturbation of order $\Delta v_R \approx 35-10 \, \mathrm{km\ s^{-1}}$ for the two armed model and $\Delta v_R \approx 100-40 \, \mathrm{km\ s^{-1}}$ in the inner regions of the Galaxy. This is not surprising since $\mathrm{Exp}[(R_0 - R)/R_d]$ is large in this region and then decays with increasing R. This result further translates into the shape of the terminal velocity curves as seen in Figures D.5b and D.6b.

The residuals in D.3 and D.4 reflect the same result. In the (c) panels where you see the deviation between the models, it is seen that the much larger radial perturbation given by the four armed model has a large effect.

All of the main conclusion drawn based on the models without the added exponential term remains the same here, which is encouraging and largely due to the fact that the exponential term is mostly relevant towards the bulge region.

Bibliography

Abadi, M. G., Navarro, J. F., Fardal, M., Babul, A., & Steinmetz, M. 2010, MNRAS, 407, 435

Adams, J. J., Gebhardt, K., Blanc, G. A., et al. 2012, ApJ, 745, 92

Baba, J., Morokuma-Matsui, K., Miyamoto, Y., Egusa, F., & Kuno, N. 2016, ArXiv e-prints

Bailin, J., Kawata, D., Gibson, B. K., et al. 2005, ApJ, 627, L17

Begeman, K., Broeils, A., & Sanders, R. 1991, Mon.Not.Roy.Astron.Soc., 249, 523

Belokurov, V., Zucker, D. B., Evans, N. W., et al. 2006, ApJ, 642, L137

Bensby, T., Feltzing, S., & Lundström, I. 2003, A&A, 410, 527

Binney, J. & Tremaine, S. 2011, Galactic Dynamics: (Second Edition), Princeton Series in Astrophysics (Princeton University Press)

Bissantz, N. & Gerhard, O. 2002, MNRAS, 330, 591

Bland-Hawthorn, J. & Gerhard, O. 2016, ArXiv e-prints

Bobylev, V. V. & Bajkova, A. T. 2014, MNRAS, 441, 142

Bosma, A., van der Hulst, J. M., & Sullivan, III, W. T. 1977, A&A, 57, 373

Bovy, J. & Rix, H.-W. 2013, ApJ, 779, 115

Bovy, J. & Tremaine, S. 2012, ApJ, 756, 89

Clarkson, W., Sahu, K., Anderson, J., et al. 2008, ApJ, 684, 1110

Clowe, D., Bradač, M., Gonzalez, A. H., et al. 2006, ApJ, 648, L109

Deason, A. J., Belokurov, V., Evans, N. W., et al. 2012, MNRAS, 425, 2840

Dehnen, W. & Binney, J. 1998, MNRAS, 294, 429

Dehnen, W. & Read, J. I. 2011, European Physical Journal Plus, 126, 55

Dobbs, C. & Baba, J. 2014, pasa, 31, e035

Dubinski, J. & Carlberg, R. G. 1991, ApJ, 378, 496

Freeman, K. C. 1970, ApJ, 160, 811

Fuchs, B., Dettbarn, C., Rix, H.-W., et al. 2009, AJ, 137, 4149

Garbari, S., Liu, C., Read, J. I., & Lake, G. 2012, MNRAS, 425, 1445

Grand, R. J. J. & Kawata, D. 2015, ArXiv e-prints

Grand, R. J. J., Kawata, D., & Cropper, M. 2012, MNRAS, 426, 167

Guo, Q., White, S., Boylan-Kolchin, M., et al. 2011, MNRAS, 413, 101

Ibata, R. A., Wyse, R. F. G., mmore, G., Irwin, M. J., & Suntzeff, N. B. 1997, AJ, 113, 634

Jurić, M., Ivezić, Ž., Brooks, A., et al. 2008, ApJ, 673, 864

Kafle, P. R., Sharma, S., Lewis, G. F., & Bland-Hawthorn, J. 2012, ApJ, 761, 98

Kazantzidis, S., Kravtsov, A. V., Zentner, A. R., et al. 2004, ApJ, 611, L73

Kleyna, J. T., Wilkinson, M. I., Evans, N. W., & Gilmore, G. 2001, ApJ, 563, L115

Koposov, S. E., Rix, H.-W., & Hogg, D. W. 2010, ApJ, 712, 260

Kuijken, K. & Gilmore, G. 1991, ApJ, 367, L9

Küpper, A. H. W., Balbinot, E., Bonaca, A., et al. 2015, ApJ, 803, 80

Lin, C. C. & Shu, F. H. 1964, ApJ, 140, 646

Lindegren, L., Lammers, U., Hobbs, D., et al. 2012, A&A, 538, A78

Malhotra, S. 1994, ApJ, 433, 687

Malhotra, S. 1995, ApJ, 448, 138

McMillan, P. J. 2011, MNRAS, 414, 2446

Minniti, D., Lucas, P. W., Emerson, J. P., et al. 2010, New Astronomy, 15, 433

Miyamoto, M. & Nagai, R. 1975, A&A, 27, 533

Moni Bidin, C., Carraro, G., Méndez, R. A., & Smith, R. 2012, ApJ, 751, 30

Navarro, J. F., Frenk, C. S., & White, S. D. M. 1996, ApJ, 462, 563

Paczynski, B. 1990, ApJ, 348, 485

Pérez-Villegas, A., Gómez, G. C., & Pichardo, B. 2015, MNRAS, 451, 2922

Piffl, T., Binney, J., McMillan, P. J., et al. 2014, MNRAS, 445, 3133

Reid, M. J. & Brunthaler, A. 2004, ApJ, 616, 872

Reid, M. J., Menten, K. M., Brunthaler, A., et al. 2014, ApJ, 783, 130

Reid, M. J., Menten, K. M., Zheng, X. W., et al. 2009, ApJ, 700, 137

Rubin, V. C., Ford, W. K. J., & . Thonnard, N. 1980, ApJ, 238, 471

Salucci, P., Nesti, F., Gentile, G., & Frigerio Martins, C. 2010, A&A, 523, A83

Schlaufman, K. C., Rockosi, C. M., Allende Prieto, C., et al. 2009, ApJ, 703, 2177

Semczuk, M., Łokas, E. L., & del Pino, A. 2017, ApJ, 834, 7

Springel, V., Frenk, C. S., & White, S. D. M. 2006, Nature, 440, 1137

Springel, V., Wang, J., Vogelsberger, M., et al. 2008, MNRAS, 391, 1685

Stadel, J., Potter, D., Moore, B., et al. 2009, MNRAS, 398, L21

Vallée, J. P. 2015, MNRAS, 450, 4277

van Albada, T. S., Bahcall, J. N., Begeman, K., & Sancisi, R. 1985, ApJ, 295, 305

van der Kruit, P. C. & Freeman, K. C. 1984, ApJ, 278, 81

Walsh, D., Carswell, R. F., & Weymann, R. J. 1979, Nature, 279, 381

Wegg, C. & Gerhard, O. 2013, MNRAS, 435, 1874

Wilkinson, M. I. & Evans, N. W. 1999, MNRAS, 310, 645

Xu, Y., Li, J. J., Reid, M. J., et al. 2013, ApJ, 769, 15

Xue, X. X., Rix, H. W., Zhao, G., et al. 2008, ApJ, 684, 1143

Zhang, L., Rix, H.-W., van de Ven, G., et al. 2013, ApJ, 772, 108

Zwicky, F. 1937, ApJ, 86, 217